



Evaluation of Pulsed & Steady Blowing Flow Control in a Slotted Leading Edge Configuration

A Senior Honors Thesis Submitted by:
Colin Patterson

IN PARTIAL FULFILLMENT OF THE REQUIREMENTS FOR A BACHELOR OF
SCIENCE IN MECHANICAL ENGINEERING

SCHOOL OF ENGINEERING
TUFTS UNIVERSITY
MEDFORD, MA
MAY 2011

Advisor: Chris Rogers
Thesis Committee: Rich Wlezien

Abstract

As aviation fuel prices continue to rise, airlines and aircraft manufacturers alike have a vested interest in reducing the fuel consumption of their aircraft. One of the promising technologies being developed to accomplish this is Active Flow Control (AFC). AFC systems are able to deliver the significant increases in maximum lift needed for the takeoff and landing portions of the mission and thereby, giving AFC the potential to reduce the size and number of flap elements required in a high-lift wing configuration.

This study focuses on an AFC system that injects high-momentum flow into the boundary layer from a slot in the leading edge. Testing was conducted in a 14inx14in wind tunnel test section. Lift and drag forces were measured directly using a 6-axis force transducer embedded within the airfoil itself. The airfoil used was a custom profile developed by Northrop Grumman and incorporates a leading edge slot at 3.5% cord. Both steady state blowing and pulsed blowing AFC were tested as part of this study. In each case the magnitude of the momentum injected was varied between 3% and 10% in the steady cases and 0.02% and .1% in the pulsed.

In the case of steady blowing, the study was able to show improvements in the maximum coefficient of lift of as much as 28% with an uncertainty of ± 0.018 . The steady blowing jets were also able to postpone stall from an angle of attack of 11° to 14° for all C_μ values greater than 3%. Pulsed blowing jets, on the other hand, were unable to generate the expected increase in maximum lift.

Acknowledgements

Throughout my undergraduate career at Tufts University I have surrounded by surrounded by an amazing group of faculty and peers who have gone out of their way to offer me guidance both in the academic arena and otherwise. I would like to thank just a few of them here. The first person I need to recognize is Dr. Rich Wlezien, my academic and research advisor, who provided me with research opportunities both in pursuit of this thesis as well as an outside project allowing me to explore my interest in wind energy. A great deal of thanks is also due to Dr. Chris Rogers who stepped up to advise me after Dr. Wlezien's departure from Tufts and who has enthusiastically guided me through my research this year. Thank you both very sincerely.

While the technical knowledge and understanding I gained from this research is by no means insignificant, my biggest take away from this thesis will be the skills in approaching an opened ended problem and working through the numerous issues encountered a long the way. I have several people to thank for their help in teaching me, quite simply, how to attack these problems. First and foremost is Alfram Bright who took spent a huge amount of his time to help me weld, solder, machine, and design my way to a working experimental setup. In the same vain, I would also like to thank Vinnie Miraglia for his help not only with this thesis but also his time helping with all my other academic pursuits. Finally, I would like to thank Reeve Dunne. Reeve started this research project and designed the first version of the airfoil used in these experiments. Reeve also headed up the project to construct the wind tunnel itself, without which none of this research would have been possible.

Table of Contents

Abstract	ii
Acknowledgements	iii
Table of Figures	v
Nomenclature & Abbreviations	vii
1.0 Introduction.....	2
1.1 Motivation.....	2
1.2 Flow Control Background.....	3
1.2.1 Passive Flow Control	4
1.2.2 Active Flow Control	6
1.3 Controlling Parameters	8
1.4 Existing Results	10
1.5 Goal and Scope of Research.	11
2.0 Experimental Setup.....	13
2.1 Wind Tunnel	13
2.2 Airfoil.....	14
2.3 Leading Edge and Slot Geometry	16
2.4 Pulsed Blowing Assembly	18
2.5 Angle of Attack Sweep Apparatus and Air Supply Configuration.....	20
2.6 Force Transduction	22
2.7 Uncertainty Analysis.....	24
3.0 Results.....	26
3.1 Steady Blowing Results	26
3.2 Pulsed Flow Control Results.....	28
4.0 Discussion	31
4.1 Steady Cases	31
4.2 Pulsed Results Discussion	34
5.0 Conclusion	36
5.1 Future Work	37
References	38
Appendix A – Additional Steady Blowing Cases	41
Appendix B – Additional Experimental Setup information	42

Table of Figures

Figure 1 - Graphical representation of the change in maximum coefficient of lift ΔCL_{max} for a given flow control excitation. [2]	4
Figure 2 - Effect of flap elements on CL for clean, slotted and multi-element configurations [5]..	4
Figure 3 - Leading edge vortex generators [15].....	5
Figure 4 - Lockheed F104 Starfighter deflected flap boundary layer flow control system [10]	7
Figure 5 - Zero mass flux Synthetic actuator jet schematic [2]	8
Figure 6 – A plot of the effect of reduced forcing frequency on a NACA 15 airfoil [6].....	11
Figure 7 - Schematic of the Tufts University wind tunnel.....	13
Figure 8 - Northup Grumman custom airfoil profile.	14
Figure 9 - Airfoil assembly including tufts array.....	15
Figure 10 - Airfoil model exploded view including all for airfoil elements, centerline plate, sensor mounting plate, the Nano25 force sensor and Sting assembly.....	15
Figure 11 - Leading edge slot geometry with two views: (a) the location of the slot along the leading edge. (b) The internal structural support of the leading edge	16
Figure 12 - Compressed air supply pipe. 10 slots measuring 1.0in X 0.15in deliver compressed air to the leading edge	16
Figure 13 - Leading Edge Calibration rig: (a) pitot 0.05in diameter tube at slot exit (b) Setra pressure transducer with pitot tube.....	17
Figure 14 - Steady blowing jet calibration curve for average jet velocity vs. input pressure.....	18
Figure 15 - Air injector manifold.....	18
Figure 16 - Sample pulsed jet velocity data showing the 62.5Hz with averaged pulsed velocities of 5.25m/s and amplitude of 0.7[m/s]	19
Figure 17 - The airfoil model attached to the ServoSystems rotary indexing head and quick disconnect sprocket assembly.	20
Figure 18 - Air supply assembly: (a) arc slots and bellows for force isolated air supply (b) slider assembly to closes unused arc slot area during AoA sweeps	21
Figure 19 - Nano25 Sensor, mounting plate and sting assembly.....	22
Figure 20 - Data acquisition and data logging schematic	23
Figure 21 - Calibration verification of the Nano25 using a known 300g load and weight calibration of the airfoil.....	24

Figure 22 - Airfoil model during testing: (a) at $\alpha=3^\circ$ with the flow still attach to 100% cord and (b) at $\alpha=13^\circ$ with the leading tufts indicating complete stall.....	27
Figure 23 - Cl vs AoA for the steady blowing cases: 5 cases of steady blowing AFC and two reference cases.....	27
Figure 24 - Cd vs. Cl for steady blowing AFC at 4 values of Cu and two reference cases	28
Figure 25 - Pulsed Blowing case Cl vs. Aoa Cu=0.2% F+:1.32.....	29
Figure 26 - Cd vs Cl plot for Pulsed Blowing AFC case.....	30
Figure 27 - Plot of $\Delta Cl_{max}\%$ vs. C_μ for the $U_\infty=16\text{m/s}$ Re: $3.56E5$ study.	31
Figure 28 - Figure of Merit plot for two cases of steady blowing AFC	33
Figure 29 - Steady Blowing $U=23.3\text{m/s}$	41
Figure 30 - Cd vs. Cl Steady Blowing cases at $U=23.3\text{ m/s}$	41
Figure 31 - Additional Airfoil profile Statistics – Northrop Grumman.....	42
Figure 32 - ATI Nano25 Drawing	43

Nomenclature & Abbreviations

Nomenclature

A_p: Airfoil plan form area

α: Angle of Attack

c: Airfoil Cord Length

C_D: $C_D = \frac{F_D}{\frac{1}{2}\rho U_\infty^2 A_P}$ - Coefficient of Drag

C_E: $C_E = \frac{W}{\frac{1}{2}\rho S U_\infty^3}$ - Coefficient of Input Energy

C_L: $C_D = \frac{F_D}{\frac{1}{2}\rho U_\infty^2 A_P}$ - Coefficient of Lift

C_μ: $C_\mu = \frac{\rho_j h U_j^2}{\frac{1}{2}\rho U_\infty^2 c}$ - Coefficient of Momentum

C_μ: $\overline{C_\mu} = \frac{2h\rho_j}{c} \left[\left(\frac{U_j}{U_\infty} \right)^2 + \left(\frac{u_j}{U_\infty} \right)^2 \right]$ - Time

dependent momentum coefficient

F_D: Force of drag – force parallel to Freestream Flow

F_L: Force of lift – force perpendicular to Freestream Flow

F⁺: $F^+ = \frac{f_e X_{te}}{U_\infty}$ - Reduced Forcing Frequency

FM: $FM = \frac{\eta}{(C_L/C_D)_{baseline}}$ - Figure of Merit

ρ: Density of fluid

h: slot height

η: $\eta = \frac{C_L}{C_D + C_E}$ - Flow control Efficiency

Q: volumetric flow rate

Re: $Re = \frac{\rho U c}{\mu}$ – Reynolds Number

U: Flow Velocity

V: Sensor Voltage

V₀: Zero-offset voltage

W: $W = \frac{1}{2}\rho Q U_j^2$ - Energy in Jet

X_{te}: Distance along cord to trailing edge from excitation slot

Abbreviations

AFC – Active Flow Control

AoA – Angle of Attack

A/D – Analogue to Digital conversion

BLC – Boundary Layer Control

FC – Flow Control

PIV – Particle Image Velocimetry

VG – Vortex Generator

WC – Water Column

1.0 Introduction

1.1 Motivation

Modern society has grown to rely on the availability of inexpensive and reliable air travel to move people and goods around the globe. The challenge for the designers of the next generation of commercial aircraft is to provide a step change improvement in fuel efficiency. The airline industry's massive exposure to jet fuel prices, as well as the impact of air travel on climate change, are already providing the needed social and economic motivation to develop fuel efficient technologies. Technologies such as high bypass ratio engines, lightweight composite materials and tip vortices drag mitigation have had allowed for significant reduction in specific fuel consumption, however, fuel still represents as much as 40% of operating costs for many airlines.[8]. These soaring costs will continue to drive the need for a new technology capable of delivering the step change improvement the industry is clamoring for.

Large commercial and cargo aircraft spend the majority of their mission at altitude, in a cruise configuration. As such, fuel efficiency is depends largely on aircraft weight and drag at cruise. One study showed that a percentage reduction in the empty operating weight of an aircraft translates 1:1 or better with a percentage savings in fuel consumption per passenger mile.[8] While cruise drag and weight optimization represents a simple goal, a major barrier exists to optimizing aircraft design for cruising conditions. In order to land and takeoff safely, aircraft must generate large amounts of lift at airspeeds far below cruising speed. In current designs this is accomplished through the use of highly mechanized, multi-element wing systems. These systems carry with them a significant penalty in weight, complexity, and manufacturing costs to the aircraft as a whole. In addition, many systems incorporate leading edge slats to further augment lift generated during takeoff and landing. Leading edge slats inherently creates surface

discontinuities along the leading edge, typically causing the boundary layer flow to become turbulent and thereby increasing skin friction drag, even while in the cruise configuration.

Due to the high penalty in weight and cost of current systems, the industry's focus has been placed on developing technologies that can provide similar increases in maximum lift and thereby allowing for a reduction in size or number of flap elements required. Active Flow Control (AFC) is one such technology and will be the focus of this study.

1.2 Flow Control Background

Flow control itself is by no means a new idea. In 1904 Prandtl published a paper demonstrating the improved attachment of flow to a solid surface when suction was used to remove the retarded flow within the boundary layer. [6] Since Prandtl's experiments, a whole host of methods have been devised to alter flow characteristics over a solid surface and favorability affect a system's performance.

In the context of airfoil performance, flow control (FC) can be used to reduce aircraft fuel consumption in two ways. The first is to use flow control to maintain laminar flow over the airfoil where it would not naturally occur. This reduces skin friction drag and can improve the performance of the aircraft at cruise. The second approach is to use FC to delay flow separation and the subsequent stall at high angles of attack. By continuing to produce lift at these very high angles, an airfoil can generate a significantly higher maximum lift as seen in Figure 1. As discussed, such a system could reduce the need for leading edge slats and flap elements. The replacement of slats could decrease skin friction drag, similar to laminar flow control, while a reduction in the number of flap elements or their size represents a significant savings in manufacturing cost and weight. This study will focus on the latter approach, where the variable of interests will be the improvement in $C_{L\ max}$ for takeoff and landing configurations.

Several techniques and flow control strategies have been shown to provide the needed increase in stall angle to generate an increase in $C_{L\max}$. In all cases, FC adds additional momentum to the boundary layer flow along an airfoil surface. The additional momentum allows the boundary layer to overcome the adverse pressure gradient and remain attached to the airfoil surface. Several FC methods operate by directly injecting high momentum flow into the boundary layer. Others create stream wise vortices to induce mixing between the free stream flow and the slower boundary layer flow. In general, these methods can be divided into two major categories: those that are passive, whose effect is a result of the natural flow over the airfoil, and active flow control, which requires an external excitation to generate the desired effect.

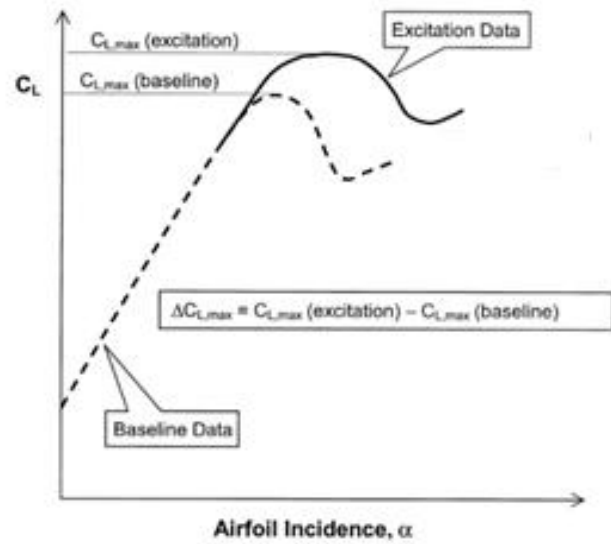


Figure 1 - Graphical representation of the change in maximum coefficient of lift $\Delta C_{L\max}$ for a given flow control excitation. [2]

1.2.1 Passive Flow Control

By far the most common form of flow control is the slotted deflected flap. These systems are passive and seen on the wings of nearly all large cargo and passenger aircraft. As shown in Figure 2 the pressure side flow of the main wing element is allowed to pass through a slot and reenergizes the boundary layer flow of the

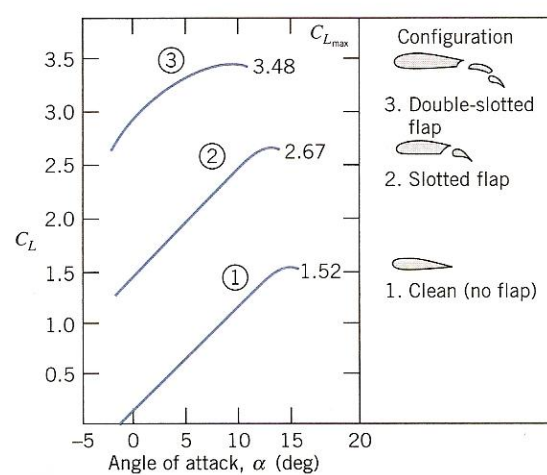


Figure 2 - Effect of flap elements on C_L for clean, slotted and multi-element configurations [5]

deflected flap. This direct injection of momentum allows the flow to stay attached to the flap despite the sharp angle of attack. In some systems multiple stages of this momentum pass-through are used to generate the needed lift increase. Not surprisingly, deflected flaps also come with a very large drag penalty. However due to the short duration of their use, this can be overcome with additional engine thrust.

While deflected flap elements are able to directly inject momentum into the boundary layer, passive flow control can also use vortex mixing to create a net addition of momentum to the flow. This technology incorporates a feature, aptly

named, called vortex generators (VG). As seen in Figure 3, they are fins extended up into the free stream forward of the separation point. VG's are used on various elements of airframes, such as the engine nacelle and wing, to reduce flow separation and wake



Figure 3 - Leading edge vortex generators [15]

size, thereby reducing drag. On an airfoil, the vortices generated by these fins mix the free stream flow with boundary layer flow and the increase in momentum within the boundary layer. As described, the increased momentum allows the flow to stay attached and higher angles of attack. The increased angle of attack drives an increase the maximum lift coefficient $C_{L\ max}$ of the airfoil.

Both of these technologies are both effective and reliable over the small portion of the flight conditions where they are needed. Over the rest of the flight, however, they can often have a detrimental effect on the airfoil's performance. VG's will typically cause a turbulent boundary layer profile and increase skin friction drag, while the weight and complexity of the multi-element flap systems can drive lower full efficiency due to weight and higher operating costs.

Because of these drawbacks, and increasing focus has been put on systems that can provide similar increases in $C_{L\max}$ during the take-off and landing portions of the mission without the negative effects throughout the remainder of the flight profile.

1.2.2 Active Flow Control

Active flow control (AFC) incorporates the same concepts of vortex mixing and direct momentum injection to increase the stall angle and prevent separation at higher angles of attack. Unlike passive systems, AFC incorporates an external excitation method that can be activated for the high-lift portions of the flight. A number of excitation methods have been developed with varying levels of utility. The first distinction to be made, however, is the difference between system that use a steady state excitation and those that use time-dependent or pulsed excitation methods.

1.2.2.1 Steady State Flow Control

Steady state ACF combats the loss of momentum due to friction in the retarded boundary layer flow by directly injecting additional high-momentum flow into the boundary layer. Most often, this is accomplish using a jet of compressed air added the boundary layer by way of a slot, or a series of slots, on the airfoil surface. The airfoils used in steady state blowing vary widely as do the geometric configuration of the slots. The most studied cases are leading edge slots and slots at the shoulder of deflected flaps. The most successful studies in term of increase in maximum lift are those conducted with the slot situated on the shoulder of a deflected flap. [6]

Similarly, Suction along the airfoil surface has also been used to remove the slow boundary layer flow and pull the high momentum, free stream flow down to the airfoil surface. In the 1960's this technology was part of a proof of concept test flights conducted by Lockheed and McDonald Douglas. A modified B-66 aircraft designated the X-21A had wings fitted with

arrays of narrow slots allowing the boundary layer flow to be removed through suction. Issues of slot contamination and clogging as well as maintenance issues were the key reason behind the technology never being implemented. [8]

Steady state hydrodynamic blowing of a deflected flap has been used in production aircraft as well. The Lockheed F104 Starfighter used a deflected flap boundary layer control system which used compressor bleed air piped out through the wings

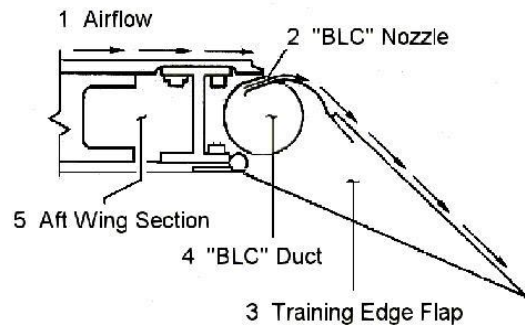


Figure 4 - Lockheed F104 Starfighter deflected flap boundary layer flow control system [10]

and over the deflected flaps. This system could only be used during landing when the flaps were extended beyond 15 degrees due to the large loss in thrust that accompanied the compressor bleed. The maintenance of the BLC system was largely to blame for discontinuation of this type of a system in future fighter models. [14]

The Starfighter and X-21A both were able to demonstrate the effectiveness of steady blowing and its improvement in lift production of a high-lift system. In both cases, however, the amount of input energy required was large, requiring significant amount of engine compressor bleed or auxiliary compressors. In order to reduce the mass flow requirements of these systems, a great deal of focus has been put on a pulsed AFC strategy able to generate similar increases in lift at far smaller levels of energy input.

1.2.2.2 Pulsed Flow Control

Instead of directly injecting the required mass into the boundary layer, Pulsed flow control instead utilizes the same vortex mixing concept seen in vortex generator technology. Jet pulses locally accelerate the boundary layer generating vortices which travel along the cord

inducing mixing of the high velocity free stream flow with the slow boundary layer flow. The result is a reenergized boundary layer that is able to overcome the adverse pressure gradient at high angles of attack and increase the angle at which separation and the subsequent stall occur.

A series of actuation mechanisms have been used to create the desired pulsing effect. Jets such as those used in steady state flow control have been paired with high-speed valves to generate the time dependence desired. It is this pulsed hydrodynamic blowing that will be investigated further in this study. It should

be mentioned, however, that a large focus has been placed on the use of zero mass flux piezoelectric actuated flaps. These flaps, as shown in Figure 5, can provide

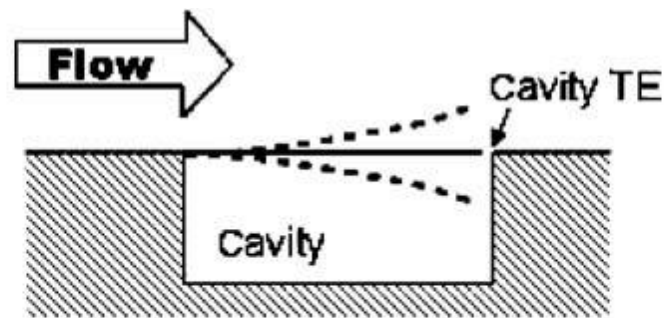


Figure 5 - Zero mass flux Synthetic actuator jet schematic [2]

the quick burst of flow to generate the mixing vortices without the need for any input air and the associated plumbing. These piezoelectric also require a small amount of energy needed to excite the flaps, given them the potential to reach very high efficiencies. [12]

The use of acoustic energy for pulsed flow control has also been well studied. These studies have shown that it is possible to positively affect airfoil performance in a wind tunnel setting. In many of these studies the input required 95 dB or more of sound to create the desired effect. [7] The practicality of the implementation of such a system aside, these acoustic input studies could not deliver the same level of lift improvement as their hydrodynamic blowing counterparts. [6]

1.3 Controlling Parameters

The performance of an airfoil and a given flow control strategy can be evaluated based on several controlling parameters. First off are the coefficients of lift and drag, C_L and

C_D respectively. These are nondimensionalized measures of the lift and drag produced by an airfoil. C_L and C_D can be thought of as the ratio of the lift or drag force to the dynamic pressure acting on plan form area of the airfoil. [5] In practice, these allow the evaluation of the lift and drag produced independent of free stream velocity, so long as the testing is conducted in a similar Reynolds number regime. The coefficient of lift is represented by:

$$C_L = \frac{F_L}{\frac{1}{2}\rho U_\infty^2 A_P} \quad (1)$$

Where F_L is the component of the force generated by the airfoil that is perpendicular to the free stream flow. Similarly, the drag coefficient is the component of the force parallel to the free-stream flow over the dynamic pressure actuating on the plan form area:

$$C_D = \frac{F_D}{\frac{1}{2}\rho U_\infty^2 A_P} \quad (2)$$

In order to characterize the flow control methods being used, one can relate the momentum added to the flow as a percentage of the momentum in the free stream. This parameter is known as the momentum coefficient and is represented by C_μ . The momentum coefficient is defined as:

$$C_\mu = \frac{\rho_j h U_j^2}{\frac{1}{2}\rho U_\infty^2 c} \quad (3)$$

Where h and c are the slot height and cord length respectively.

Pulsed flow control can be described by two parameters. The first of these is a time dependent momentum coefficient where steady state jet velocity and average pulse velocity are incorporated as shown in equation 4.

$$\overline{C_\mu} = \frac{2h\rho_j}{c} \left[\left(\frac{U_j}{U_\infty} \right)^2 + \overline{\left(\frac{u_j}{U_\infty} \right)^2} \right] \quad (4)$$

The second parameter used to describe unsteady flow control is known as the reduced forcing frequency (F^+). The forcing frequency effectively describes the number of pulses over the cord at a given instant.

$$F^+ = \frac{f_e X_{te}}{U_\infty} \quad (5)$$

1.4 Existing Results

Both steady and pulsed blowing flow control strategies have been shown to produce favorable max lift characteristics for a given airfoil. In the case of deflected flap configurations, both steady and pulsed blowing were able to produce improvements from 40% up as much as 120% $\Delta C_{L\max}$ in several cases. These pulsed blowing systems required C_μ values in the neighborhood of 0.15% to 2%. Similar steady blowing systems required a C_μ of at least 3% to as much as 10% to achieve similar results. [6, 16]

In leading edge configurations, the increases in $C_{L\max}$ were notably less than their deflected flap counterparts. Here again, steady and pulsed blowing were able to achieve similar increases in $C_{L\max}$, however in both cases improvements were between 20% and 30% $\Delta C_{L\max}$. The pulsed cases were able to accomplish these gains with C_μ values as low as 0.01% and up to 2%, while the steady blowing cases again required momentum coefficient values of between 3%-10%. [6]

In the case of steady blowing, both very low and very high C_μ values have been shown to be detrimental to the flow. In the case of low C_μ , this is typically due to the jet velocity being close to or lower than the free stream velocity. As such, these pulses actually decrease the

boundary layer flow momentum. At very high C_μ values, the momentum of the jet can ‘push’ the flow away from the airfoil surface, effectively forcing separation at the slot location. [6, 2]

Many studies also examine the role of the reduced forcing frequency (F^+) on the performance of pulsed ACF systems. The effective ranges vary from between $0.3 < F^+ < 4$. As seen in Figure 6, the improvement in C_L comes to a sharp peak when F^+ is varied independently. [6]

One of the key observations in looking at any compilation of AFC data is the high degree of variability and sensitivity of the results to the specific conditions of the test. The specific qualities of the pulsing actuators, the curvature of the airfoil at the slot location, Reynolds number and 3-dimensional effect can all have a significant impact on results and alter optimum reduced forcing frequency and momentum coefficient values. This high degree of variability and sensitivity to operating conditions continues to drive research to better understand and optimize AFC systems.

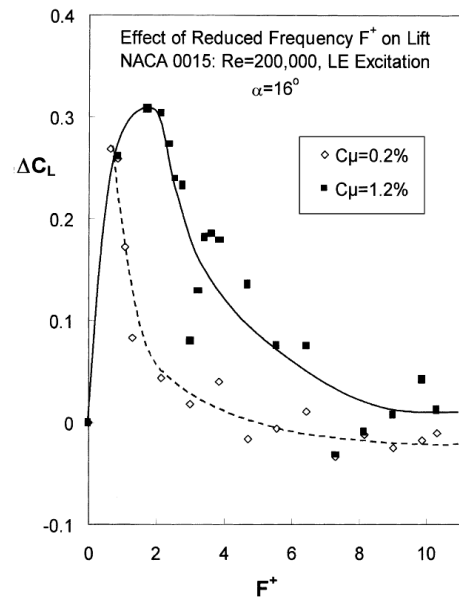


Figure 6 – A plot of the effect of reduced forcing frequency on a NACA 15 airfoil [6]

1.5 Goal and Scope of Research.

The following study examines the use of both steady and pulsed hydrodynamic blowing from a leading edge slot. The focus will be to look at the lift and drag data to determine the ability of this AFC method to increase $C_{L\max}$ and the stall angle of the custom Northrop Grumman airfoil. The experiments will be performed under several different sets of conditions but can by no means be interpreted as a complete study or optimization of the parameters

involved. Instead, the study will consider impact of variations in $\overline{C_\mu}$ and C_μ under a set of conditions shown to be effective in many AFC experiments.

2.0 Experimental Setup

2.1 Wind Tunnel

The Tufts University wind tunnel used in these experiments has a 42 inch long test section with a 14in square cross section. The tunnel is a closed loop system and uses an in-line 5hp fan capable of generating free stream flow up to 25 m/s in the test section. For the majority of the testing done, the tunnel was operated at $U_{\infty}=16.5$ m/s to generate the C_{μ} values desired. The tunnel operating temperature can increase to as much as 40°C during extended continuous operation. As such, operating temperature was monitored using an Omega class B 0.0385PT RTD mounted at the inlet to the test section. Care was taken to limit test run times to ensure tunnel temperature change did not change the Reynolds number beyond the desired region of $2.5 \times 10^5 < Re < 5.0 \times 10^5$. Figure 7 shows an assembly schematic of the wind tunnel as a whole.

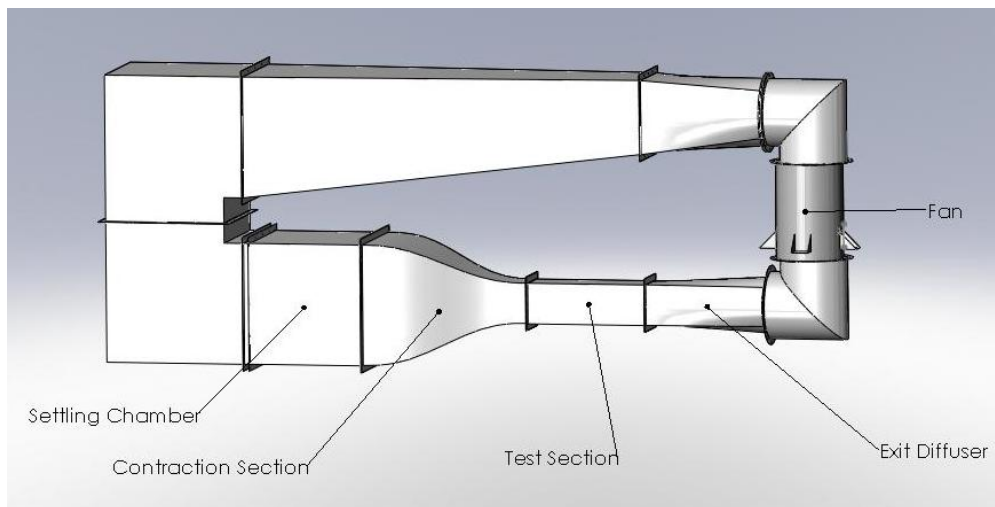


Figure 7 - Schematic of the Tufts University wind tunnel

Free stream velocities were measured using a Model 160-12 Dwyer Pitot Probe. Pressure differentials from the Pitot Probe were determined using a Setra Model 264 1-10in WC pressure transducer and recorded as part of the data acquisition system as described in section 2.6. At this point in time no thorough analysis had been done to characterize the tunnel's free stream turbulence, however work being done in parallel with this research suggests a turbulence intensity of approximately 1.5% based on a PIV study of the free stream flow done using a New Wave PIV system and Insight 3G version 9.0 by TSI incorporated.

2.2 Airfoil

Northrop Grumman Corporation provided the custom airfoil profile used in this research. The profile features a relatively sharp leading edge and a max thickness at 41% cord. Figure 8 shows this profile. Additional information on the airfoil profile is shown in Appendix B.

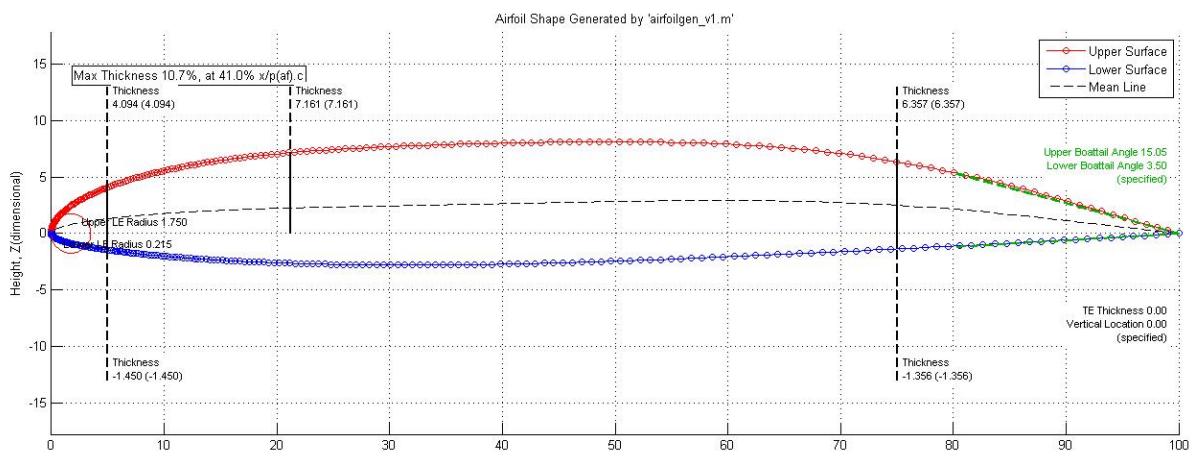


Figure 8 - Northup Grumman custom airfoil profile.

The airfoil model was created out of ABS M-30 plastic using a FORTUS 360mc 3D printer from Stratasys. The model has a cord length of 14 inches and a resulting max thickness of 1.5in. The model was designed out of four separate segments: two center elements, a leading edge, and the trailing edge. A great deal of care was taken to ensure that the model could be

assembled and disassembled repeatedly with different leading and trailing edge configurations as required.



Figure 10 - Airfoil model exploded view including all for airfoil elements, centerline plate, sensor mounting plate, the Nano25 force sensor and Sting assembly

An aluminum mounting plate joins the two center elements and provides a flat and rigid surface for the force sensor mounting plate. Figure 9 shows the exploded view of the airfoil assembly as well as the sting and sensor assembly.

The sensor passes through the left-center module and mounts to the centerline plate. The sensor itself will be discussed in section 2.6. The airfoil elements were assembled, sanded and polished to get the desired level of surface smoothness.

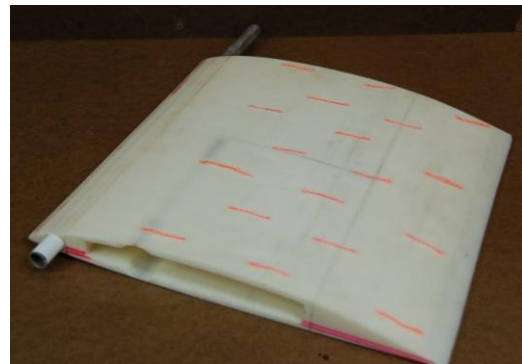


Figure 9 - Airfoil assembly including tufts array

Finally, an array of tufts were added to the suction side of the airfoil, as seen in Figure 10, to provide some flow visualization feedback to serve as a check against the lift and drag data.

2.3 Leading Edge and Slot Geometry

The geometry of the slots used to inject mass into the flow is one of the major factors that is largely ignored in AFC studies. While many slot geometries feature a larger diffusion section followed by a quick contraction as the jet is ejected into the flow, the angle at which the jet is

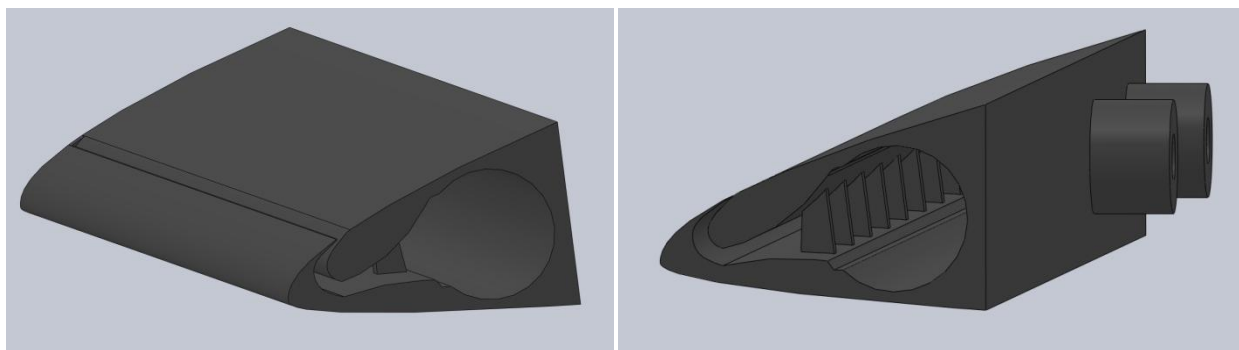


Figure 11 - Leading edge slot geometry with two views: (a) the location of the slot along the leading edge. (b) The internal structural support of the leading edge

injected into the flow is seldom discussed in the literature. The slot geometry evaluated in this study focused on creating a highly tangential jet. The argument behind this idea being that the tangential flow would provide the greatest momentum addition without ‘pushing’ the flow off the airfoil surface potentially causing premature separation. Figure 11 shows two cross sections of slot geometry used.

Compressed air is supplied to the slot by way of a thin-walled aluminum pipe, shown in Figure 12, slotted to deliver the flow. Additionally, two layers of 34% open area mesh was



Figure 12 - Compressed air supply pipe. 10 slots measuring 1.0in X 0.15in deliver compressed air to the leading edge

placed over the air delivery pipe to develop a pressure drop across the pipe slots in an effort to deliver a more uniform flow along the span of the model.

For the steady blowing cases, the compressed air supply could be provided to the leading edge directly from regulated shop air. The flow was pressure regulated by a SpeedAir 150psi rated regulator which could deliver up to 800kPa from the shop air system. Calibration of the leading edge jet to the regulator pressure was done through the use of a 0.05in diameter pitot tube, shown in figure 13. The pitot tube pressure differential was measured by a Setra Model 264 differential pressure transducer with a range of 0-1.0in WC. A/D conversion and datalogging system are discussed in section 2.6. A LabVIEW data was written specifically for the leading edge calibration. It was responsible for the voltage to velocity based on equation 6.

$$U_j = \sqrt{\frac{2 \left[0.2(V - V_0) \left(\frac{1Pa}{249.17WC} \right) \right]}{\rho_{air}}} \quad (6)$$

The jet velocity was measured at 10 locations along the span and averaged. Figure 13 shows the setup of the calibration stand. Figure 14 shows the range of steady state leading edge jet velocities capable of being produced by this system.

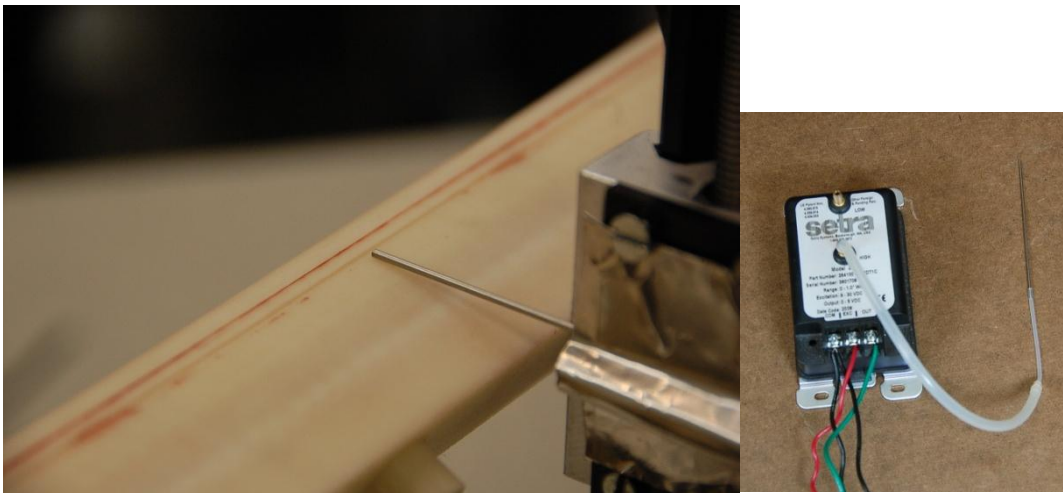


Figure 13 - Leading Edge Calibration rig: (a) pitot 0.05in diameter tube at slot exit (b) Setra pressure transducer with pitot tube.

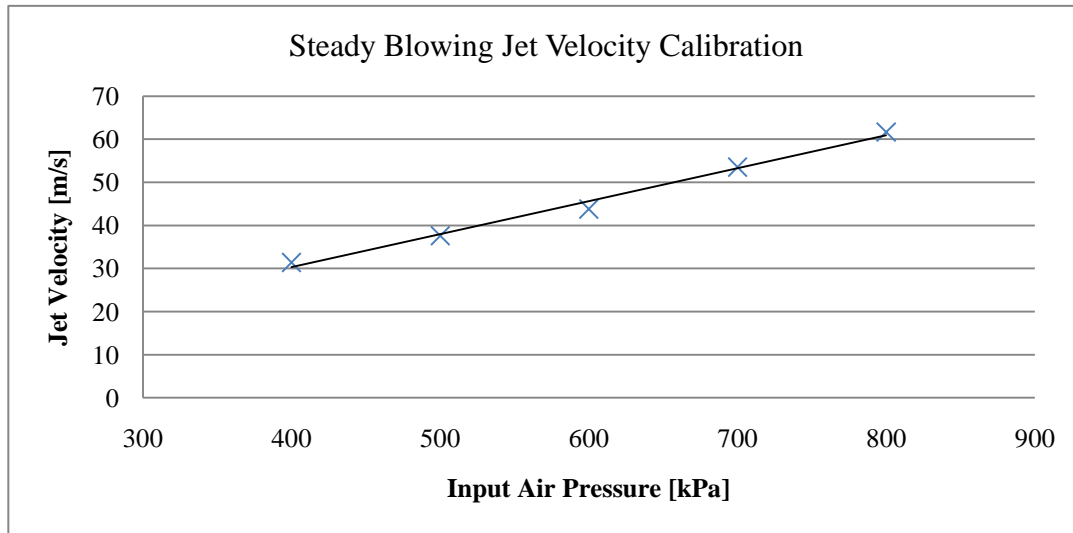


Figure 14 - Steady blowing jet calibration curve for average jet velocity vs. input pressure

In the pulsed blowing cases, the same leading edge calibration rig was used. The LabVIEW data logging script was modified to record the duty cycle and frequency in addition to input pressure. The code also determined the amplitude for the pulses and evaluated the true frequency of the pulsing. Due to the large pressure drop across the pulsing mechanism, discussed in Section 2.4, the mean jet velocities at 800kPa were on the order of 6 m/s with actual mean velocity depending strongly on the frequency of the input.

2.4 Pulsed Blowing Assembly

The pulsed blowing assembly took advantage of the same shop air supply as the steady cases. In order to deliver the rapid pulsing, an automotive fuel injector manifold was placed inline with the shop air supply. The fuel injectors proved an effective way to deliver repeatable, high frequency pulsing over an



Figure 15 - Air injector manifold.

extended test period. Because of the significant pressure drop across the injectors, mean jet velocities were a full order of magnitude lower than their steady blowing cases counter parts. Despite this, the assembly, shown in Figure 15, delivered measured mean slot velocities corresponding to the desired $\overline{C_\mu}$ values ranging from 0.1% to 0.02%. Additionally, the fuel injector manifold produced pulsed blowing rates in excess of 60Hz, corresponding to Effective F^+ values between 1 and 2 at a free stream velocity of 16.25m/s. Figure 16 shows a sample case of the leading edge calibration data for a 62.5Hz pulse. As can be seen, the fuel injectors provide an excellent frequency response, however the amplitude of the pulses are less than 1m/s. This low pulse amplitude is the key drawback to the large amount of pressure drop inherent to this air delivery method. The impact of the low pulse amplitude will be discussed further in Section 4.2.

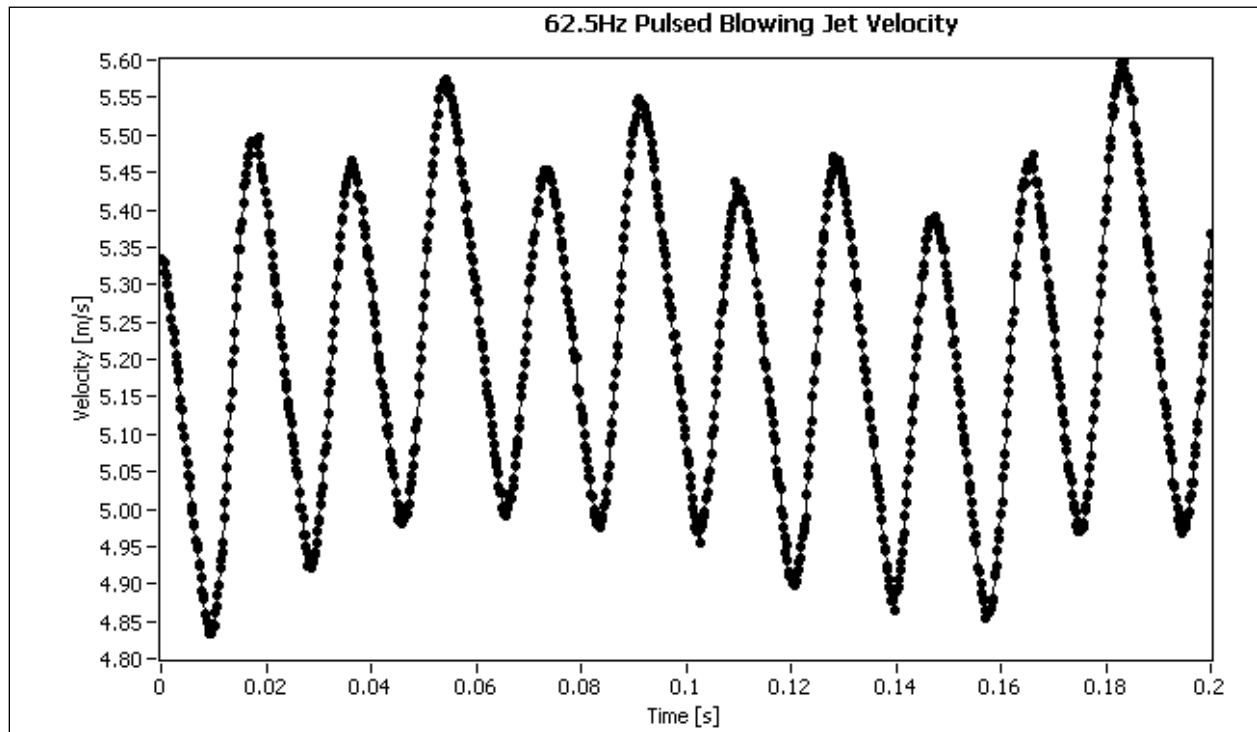


Figure 16 - Sample pulsed jet velocity data showing the 62.5Hz with averaged pulsed velocities of 5.25m/s and amplitude of 0.7[m/s]

2.5 Angle of Attack Sweep Apparatus and Air Supply Configuration

The ability to generate the desired lift and drag curves for different AFC conditions relied heavily on the ability to rotate the model through an angle of attack (AoA) sweep repeatably and easily. The use of an internal force transducer also required that lift and drag forces be balanced by the sensor-sting assembly only. As such, the compressed air supply to the leading edge needed to be isolated from the airfoil itself so no artificial forces would be imparted on the transducer. These conditions would need to remain true throughout a full AoA sweep from -5° to 30° .

A ServoSystems Model 10R90 rotational indexing head with a 10in diameter mounting plate provided the ridged base for the AoA sweep assembly. The indexing head featured a 0.1° step size. To affix the sting to the indexing head, an industrial sprocket-quick disconnect style mount was attached the face of the indexing head. As shown in Figure 17, the indexing head and quick disconnect assembly gave the sting a very rigid mounting point and the ease of the quick

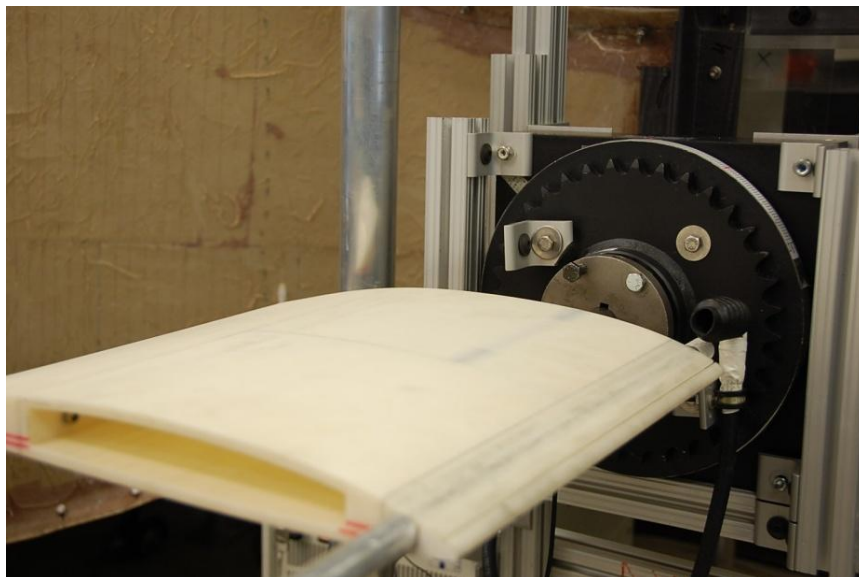


Figure 17 - The airfoil model attached to the ServoSystems rotary indexing head and quick disconnect sprocket assembly.

disconnect system allowed the airfoil to be installed in the tunnel with minimal risk of overloading the fragile force transducer.

To supply the compressed air to the leading edge without imparting any artificial forces on the airfoil, 1 in rubber bellows were employed to separate forces in the air supply hoses from the aluminum supply pipe. The aluminum pipe passes through arc slots cut in the test section walls and affixed to the bellows. On both sides of the tunnel, the supply hoses were supported by the AoA sweep assembly. Finally, the arc air supply slots in the test section walls needed to be covered at each angle of attack except for the small portion left open for the supply pipe. To do this, a sliding mechanism was developed that could move in parallel with the airfoil and cover the slots without imparting any forces on the airfoil. The bellows, arc slots and slider assembly are shown in Figure 18.

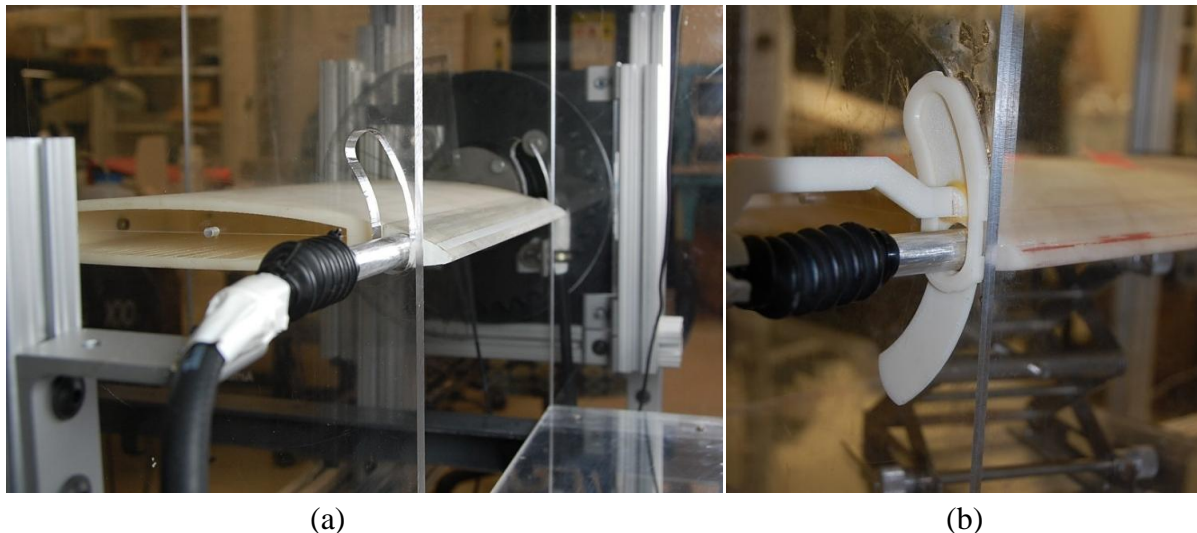


Figure 18 - Air supply assembly: (a) arc slots and bellows for force isolated air supply (b) slider assembly to closes unused arc slot area during AoA sweeps

2.6 Force Transduction

The force sensor used in for this study was the Nano25 6-axis force transducer produced by ATI industrial Automation. The Nano25 has a diameter of 0.98 inches allowing it to fit within the airfoil model while maintaining sufficient wall thickness to not risk the model strength. Figure 19 shows the Nano 25 as part of the sting and mounting plate assembly. The sting and mounting plate are custom parts designed to interface the Nano 25 with the airfoil. The Nano25 interface is

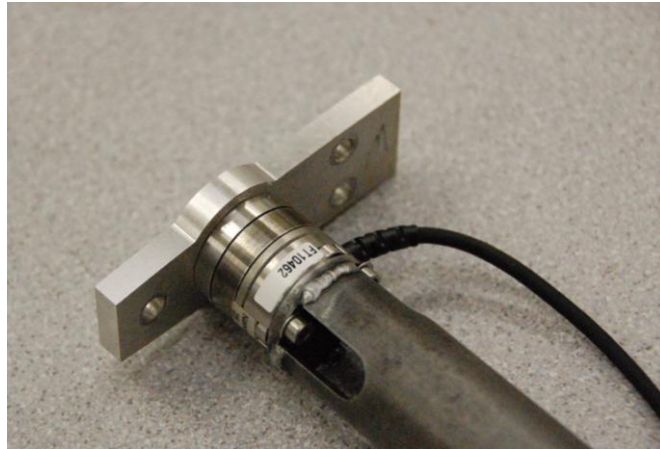


Figure 19 - Nano25 Sensor, mounting plate and sting assembly

shown in additional detail in Appendix B. As discussed in Section 2.2 the mounting plate meets the centerline plate of the airfoil and can be easily inserted and removed without any need to disassemble the airfoil model itself. This was a critical feature of the model design as the sensor was susceptible to overloading during handling. In this design, the sensor could be removed and safely stored while work such as sanding or calibration of the leading edge was done.

The Nano25 output was a six channel ± 10 V analogue signal. A pair of National Instruments NI 9215 cards and a NI cDAQ-9172 chassis handled the A/D conversion of the six channels of force data as well as a single channel of output from the Seta Pressure transducer used to evaluate the free stream pitot tube response. One additional NI 9217 card was used to evaluate the RTD temperature probe output. The composite 8 channel digital signal was handled by a custom LabVIEW program to evaluate the data and determine and log the desired values.

Figure 20 shows the schematic of the data acquisition system used in this study.

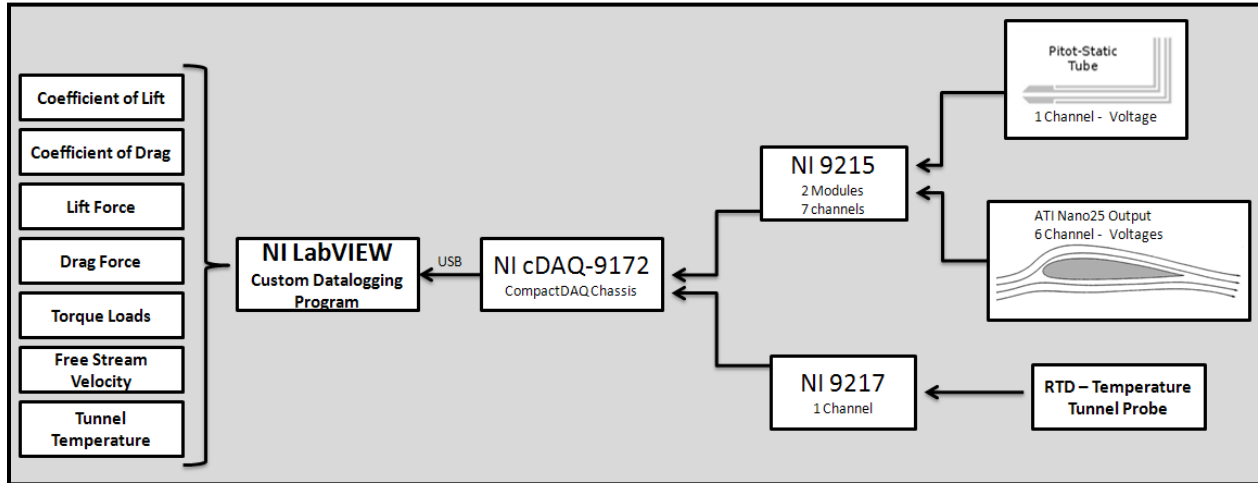


Figure 20 - Data acquisition and data logging schematic

A calibration file provided by ATI Industrial Automation handled the conversion from strain gauge voltages to physical forces. The Nano 25 contains 6 strain gauges arrayed in geometric configuration that allows physical forces to be determined, however, each physical forces is function of several strain gauge responses. As a result, if any of the gauges was outside of its operational range, all of the physical force data was invalid. As such, the LabVIEW program was designed alert the user when any of the strain gauges approached the end of its range. This feature was often used during the setup procedure as well to ensure no unexpected loads were imparted on the airfoil and the Nano25.

Finally, the Nano25 calibration was validated by applying a known load to the mounting plate and rotating the sensor through 360 degrees. Figure 21 shows the resulting data for AoA

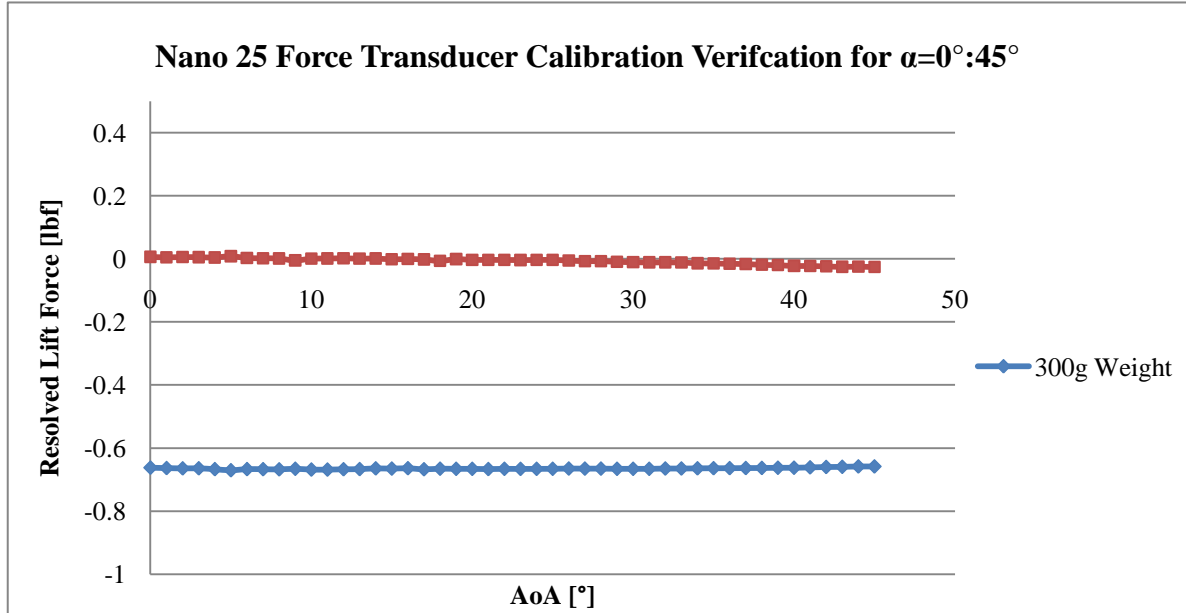


Figure 21 - Calibration verification of the Nano25 using a known 300g load and weight calibration of the airfoil between 0 and 45 degrees for both a 300g weight (0.661 lbf) as well as the calibration sweep of the airfoil model itself. In the case of the airfoil model, the data shows the calibrated sweep in which the weight of the airfoil itself is removed such that all forces measured are a result of the aerodynamic lift and drag. As can be seen in figure, the Nano25 and the DAQ system used resulted in a drift over time of as much as ± 0.05 lbf.

2.7 Uncertainty Analysis

The primary source of experimental uncertainty, within the pre-stall region considered in this, study was the Nano25 sensor itself. A combination of electronic noise in the analogue signal and a slow zero point drift over time complicated the data collection process. In order to mitigate these issues each measurement at a given angle of attack was averaged over a 5 second interval. Furthermore, a new calibration run was set at the beginning of each group of alpha sweeps to help minimize the impact of the sensor drift. As a result, the measurements were valid to the

uncertainties shown in Table 1. Nominal values here are determined by the average value in the 16.25 m/s free stream alpha sweeps from zero degrees to stall.

Table 1 - Measurement Uncertainties

Measured Value	Nominal Value μ	Uncertainty σ	Coefficient of Variation C_x
$\mathbf{F_L}$	4.57 lb	$\pm 0.05\text{lbf}$	$C_{Fl} = 0.011$
$\mathbf{F_D}$	0.322 lb	$\pm 0.05\text{lbf}$	$C_{FD} = 0.155$
$\mathbf{U_\infty}$	16.25 m/s	$\pm 0.11\text{m/s}$	$C_U = 0.007$

Using the propagation of error formulae presented in *Shigley's Mechanical Engineering Design*, the uncertainty in the variables of interest, namely C_L and C_D , can be estimated by the following formulation [1]:

$$\sigma_{U^2} = 2C_U(\mu_U)^2 \left[1 + \frac{1}{4}C_U^2 \right] \quad (7)$$

$$\mu_{U^2} = (\mu_U)^2 [1 + C_U^2] \quad (8)$$

Equations 11 and 12 estimate the uncertainty and mean as part of the velocity squared term. This is then applied to equations 13 and 14 to estimate the uncertainty in C_L and C_D :

$$\sigma_{C_L} = \left(\frac{2}{\rho A_p} \right) \left[\frac{\mu_{F_L}}{\mu_{U^2}} \left(\frac{C_{Fl}^2 + C_U^2}{1 + C_U^2} \right) \right] = \pm 0.018 \frac{m}{s} \quad (9)$$

$$\sigma_{C_D} = \left(\frac{2}{\rho A_p} \right) \left[\frac{\mu_{F_d}}{\mu_{U^2}} \left(\frac{C_{Fd}^2 + C_U^2}{1 + C_U^2} \right) \right] = \pm 0.011 \frac{m}{s} \quad (10)$$

These values nicely capture the variation between identical runs in the final data. Furthermore, it shows the effects of AFC in the steady blowing cases, discussed in 3.1, were well outside the magnitude of this uncertainty.

3.0 Results

Testing for this study was conducted in three phases: The first examined the airfoil without the assistance of AFC and is represented in the results by the ‘slot taped’ curves. The second phase encompassed all the steady blowing cases and the final phase of testing examining the pulsed blowing cases. Each set of tunnel runs was preceded by a weight calibration run to help mitigate the effects of sensor drift and each alpha sweep was conducted from 0 degrees AoA to stall.

3.1 Steady Blowing Results

A baseline case was established for the airfoil by sealing the leading edge slot with a thin tape and sanding the surface flush. Testing was done at a series of Reynolds numbers however this analyses will focus on the free stream velocity of 16.25m/s and a resulting Reynolds number of 3.56×10^5 . For reference, an additional case at Reynolds numbers 4.94×10^5 have been included in Appendix A.

In addition to the direct force measurements, tufts were also used to understand and visualize the flow conditions. For the purposes of these experiments the airfoil was considered ‘stalled’ when the leading row of tufts indicated the flow had separated. Figure 22 shows two cases of the tufts response. Due to the sharp leading edge, the stall of the airfoil was quite abrupt and obvious. For the clean, no AFC cases, the airfoil stalled at 11° and was completely separated and chaotic at 12° . The visual indication of stall was also nicely reflected in the drag data, discussed below.

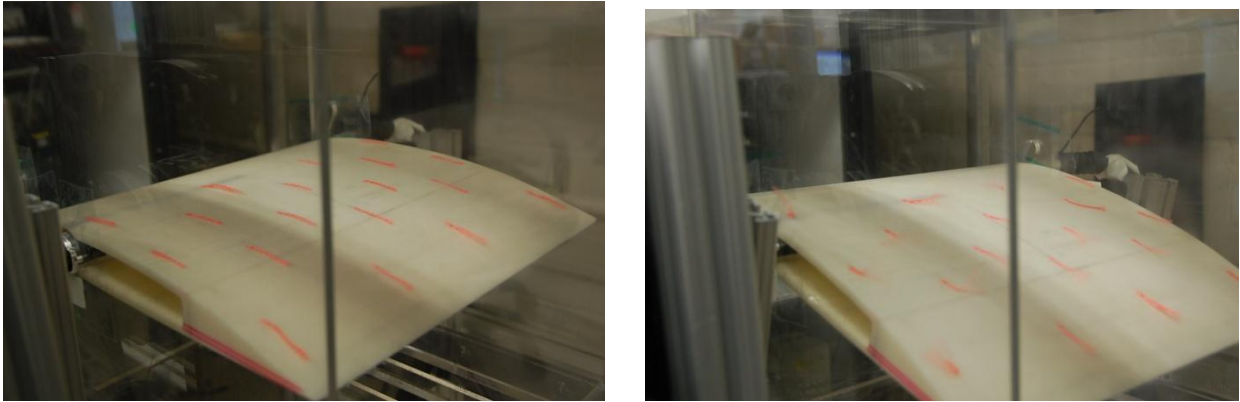


Figure 22 - Airfoil model during testing: (a) at $\alpha=3^\circ$ with the flow still attach to 100% cord and (b) at $\alpha=13^\circ$ with the leading tufts indicating complete stall

Figure 24 shows the lift vs. angle of attack data for the steady blowing cases. For each case the data has been truncated at stall as determined by the separation of the flow at the most forward row of tufts. The ‘no blowing’ curve shows the performance of the airfoil without any

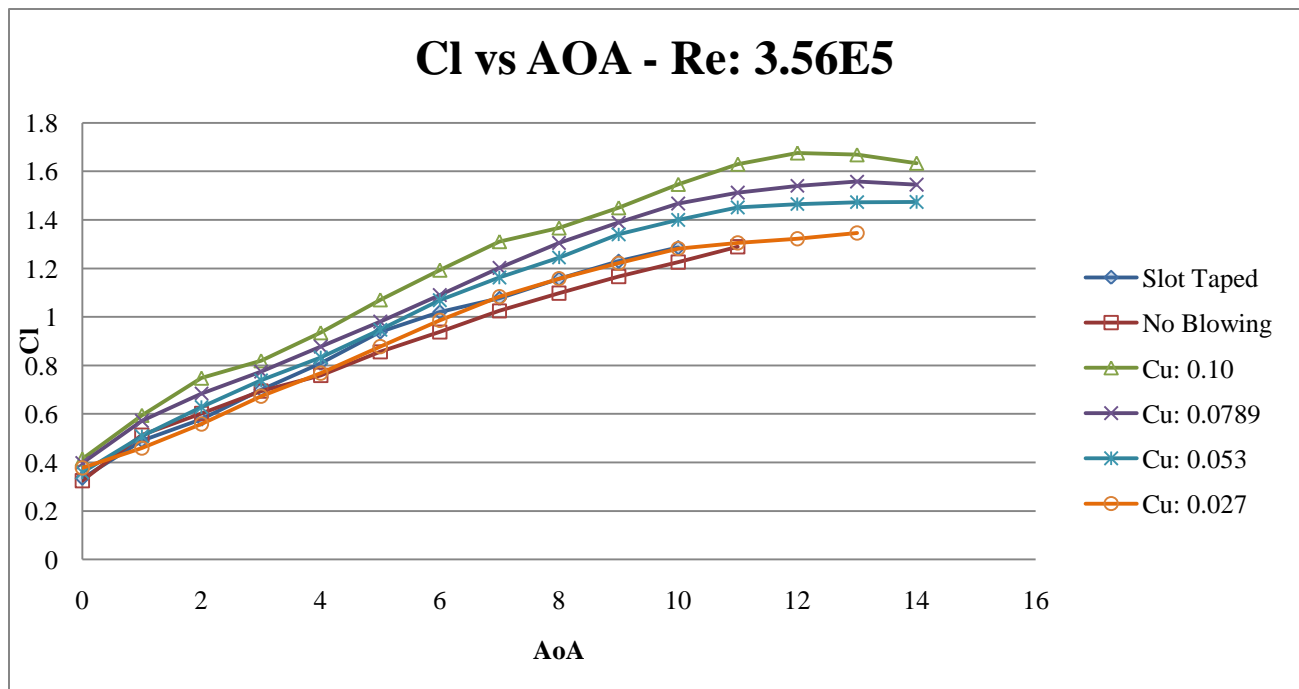


Figure 23 - C_l vs AoA for the steady blowing cases: 5 cases of steady blowing AFC and two reference cases.

AFC and slot exposed. As seen in the plot, C_μ values greater than 2% were able to postpone stall from 11° to 14° .

The study also looked at the effects of flow control on drag. Figure 24 plots the coefficient of drag vs. the coefficient of lift for each of the pre-stall angles of attack. The band of 4 flow controlled cases start with a lower coefficient of drag that the no flow control cases. The increase in drag of the baseline cases is more gradual while the AFC cases show a more constant

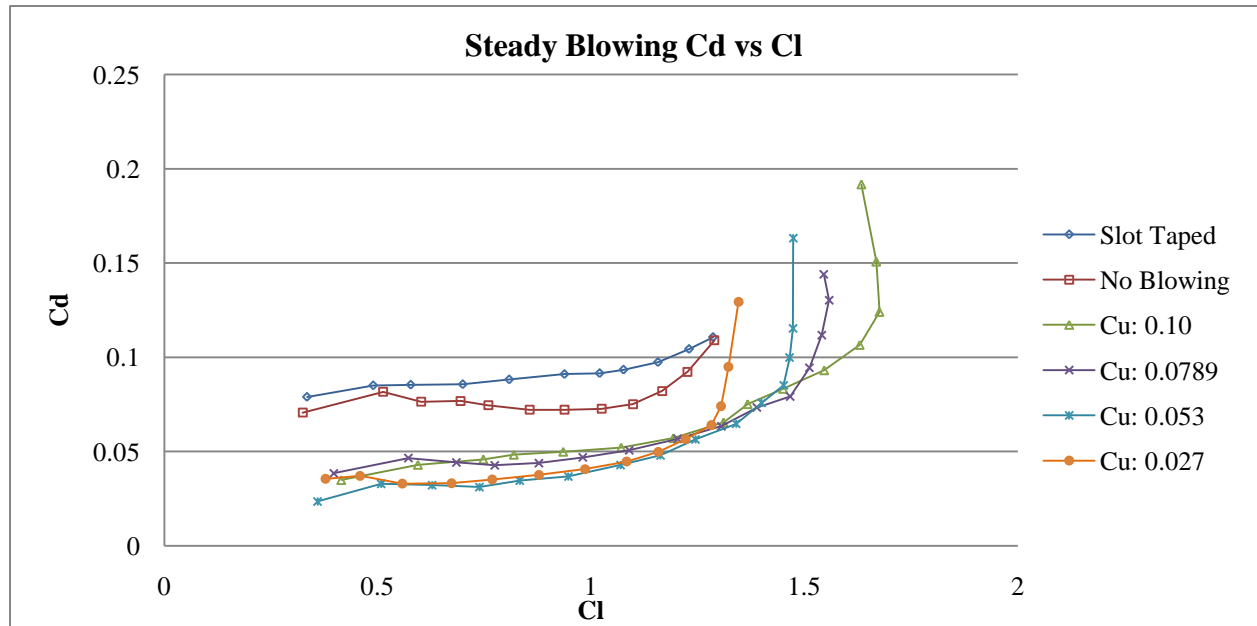


Figure 24 - Cd vs. Cl for steady blowing AFC at 4 values of Cu and two reference cases

coefficient of drag until much higher angles of attack, and then experience a sharp spike in drag in the last two to three degrees preceding stall. It should also be noted that the case in which the slot is not covered has a lower coefficient of drag after an angle of attack of 5 degrees. This case shows a similar spike in drag in the last two to three degrees of the sweep.

3.2 Pulsed Flow Control Results

The pulsed blowing testing was conducted using the same procedure as the steady cases. Here again the analysis will focus on the case of a free stream velocity of 16.25m/s and a Reynolds number of 3.56×10^5 .

Figure 25 shows the coefficient of lift vs. angle of attack plot for the pulsed case. This test was conducted with a C_{μ} of 0.2% and a reduced forcing frequency of $F^{+}=1.23$. These values correspond to an average jet velocity of 6.25 m/s and a pulsing frequency of 62.5Hz. As one can see, the plot shows a slight increase in coefficient of lift beyond 5° , however these values are well within the uncertainty of the experiment. The results across all of the pulsed cased testing showed a similar lack on performance and certainly did not show any postponement of stall.

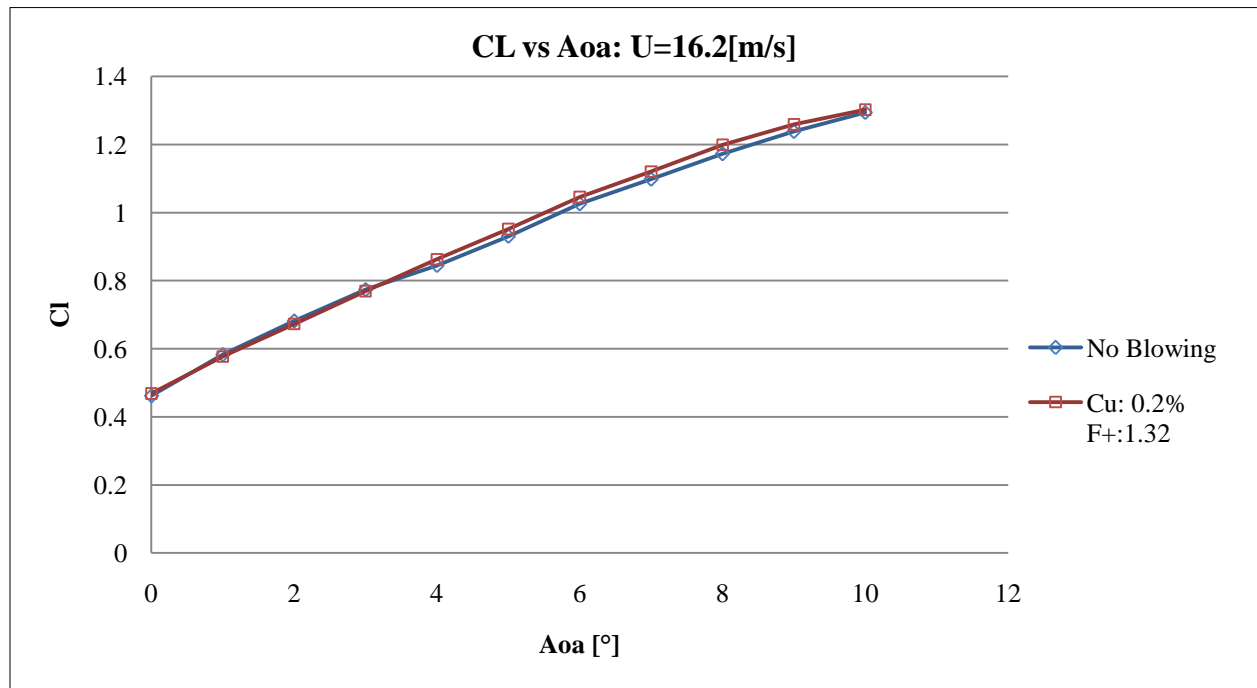


Figure 25 - Pulsed Blowing case Cl vs. Aoa $C_{\mu}=0.2\%$ $F^{+}:1.32$

Drag in the pulsed cases was equally unchanged by the use of AFC. Figure 26 shows the coefficient of drag versus coefficient of lift for the same pulsed blowing case.

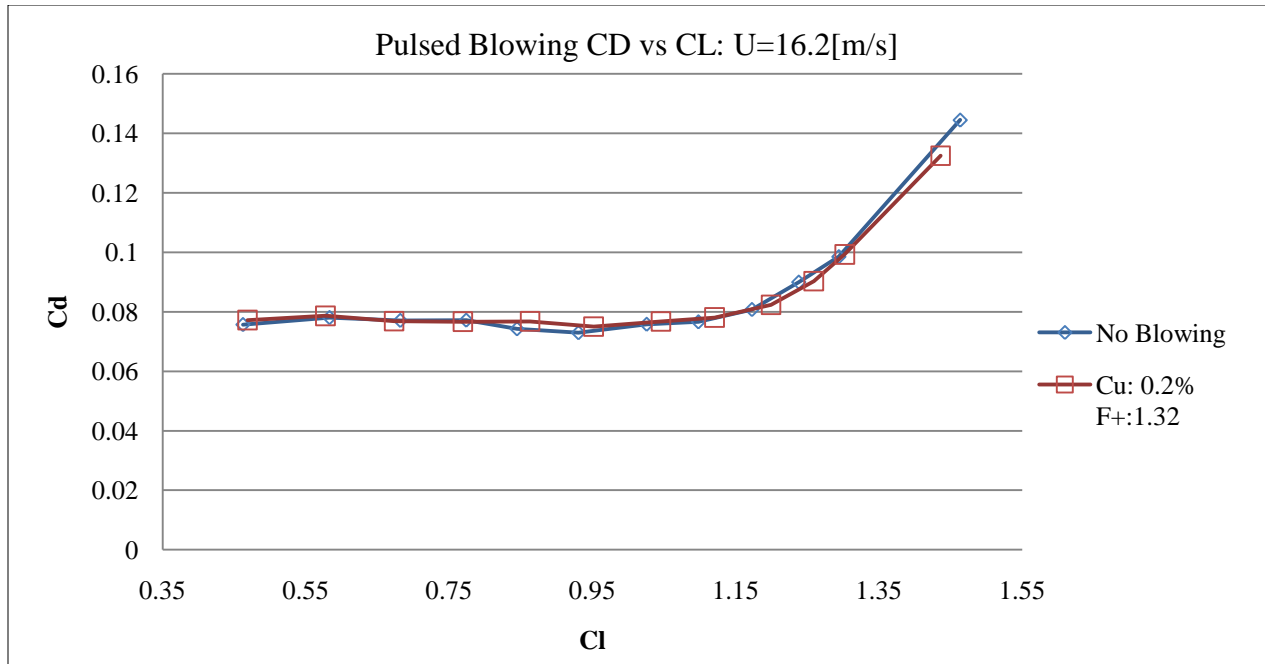


Figure 26 - Cd vs Cl plot for Pulsed Blowing AFC case

Several additional cases were run at lower free stream velocities, and therefore higher values of $\overline{C_\mu}$. Even at the increased values of $\overline{C_\mu}$ the pulsed blowing system was unable to generate an increase in performance. It should be noted, however that due to the lower free stream velocity, the Reynolds number of these tests was below 2.0×10^5 which is the approximate threshold at which turbulence naturally occurs. Due to this discrepancy in test conditions these results will not be presented here. Section 4.2 will discuss potential causes for the lack of effectiveness of these pulsed cases.

4.0 Discussion

4.1 Steady Cases

The results of the steady blowing cases were very encouraging. The slots taped cases were able to replicate the 11° degree stall angle and $1.3 C_{L\max}$ found in a Northrop Grumman study of the same airfoil profile. The application of a steady jet from the leading edge of the airfoil was able to increase the max lift notably. Figure 27 shows the percent increase in $C_{L\max}$ for each case discussed in section 3.1 and shown in Figure 23. One can see how C_μ values as low

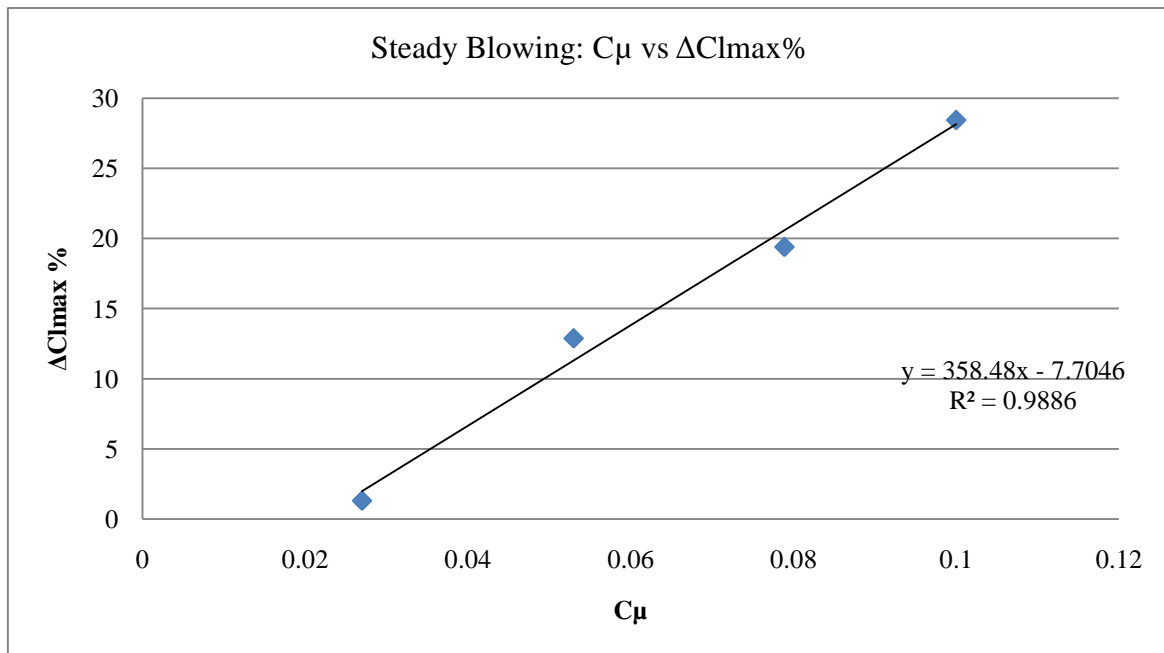


Figure 27 - Plot of $\Delta C_{l\max} \%$ vs. C_μ for the $U_\infty=16\text{m/s}$ $Re: 3.56E5$ study.

as 2% had little to no effect on $C_{L\max}$, while C_μ values of 10% were able to generate improvements in $C_{L\max}$ of nearly 29% over the no flow control baseline. As shown in the figure, the $\Delta C_{L\max}$ versus C_μ curve forms a surprisingly linear relationship. While other studies have found that steady blowing can degrade at C_μ values higher than 8%, this system continued to show improvement up to the maximum C_μ test of 10%. This is likely due to the highly tangential and attached nature of the flow emitted from the leading edge slot.

The steady blowing AFC was also able to reduce the coefficient of drag during pre-stall flight conditions. This is likely a result of two primary mechanisms. The first is simply the thrust from the steady state jet being pushed along the cord. The thrust effect accounts for the flow-controlled cases being in a separate and lower band of C_D values. Secondly, the flow-controlled cases demonstrate a lower and more constant level of drag than the baseline cases up until stall. The ability of the steady jet to postpone separation of the flow accounts for these lower and steadier drag values. The result is that when the adverse pressure gradient does overcome the additional momentum provided by the flow control jet, the separation and stall of the airfoil is far more abrupt and results in the quick spike in drag seen in C_D vs. C_L curves of the flow controlled cases.

An improvement in $C_{L\max}$ of 28.4% is largely consistent with steady blowing, leading edge studies done under similar conditions. [6,2] While these results demonstrate the potential of active flow control, an improvement of 29% can simply not compare to the 100+% improvements that can be achieved using multiple element airfoils. A steady blowing technology could certainly be used in conjunction with a multiple element airfoil, however, as seen in the F104 Starfighter, this adds a large amount of equipment and maintenance concerns to an already complex system.

Lastly, concerns over the efficiency of delivering such a large mass flow rate along a wing certainly limit the utility of these steady blowing results. The need for C_μ values on the order of 10% drives down the efficiency of the flow control method to well under 1.0. The power required can be estimated by Equation 7 making the significant assumption of 100% efficiency compressed air delivery:

$$W = \frac{1}{2} \rho Q U_j^2 \quad \text{where } Q = U_j (h \cdot l) \quad (11)$$

One can then use the input power coefficient to normalize this power by the energy of the free stream over the plan form area of the airfoil [12].

$$C_E = \frac{W}{\frac{1}{2}\rho S U_\infty^3} \quad (12)$$

The airfoil power efficiency can then be defined as [12]:

$$\eta = \frac{C_L}{C_D + C_E} \quad (13)$$

Finally, the Figure of Merit can be expressed as the ratio of power efficiency to aerodynamic efficiency [12]:

$$FM = \frac{\eta}{(C_L/C_D)_{baseline}} \quad (14)$$

Figure 28 shows the figure of merit values vs. the coefficient of lift for two different cases of steady blowing. The result is a peak value of 0.54 in the case of the $C_\mu=0.05$. These values well under 1.0 demonstrate one of the key short coming of steady blowing AFC and the draw to systems that can provide the same improvements in lift without the need for such massive mass flow rates.

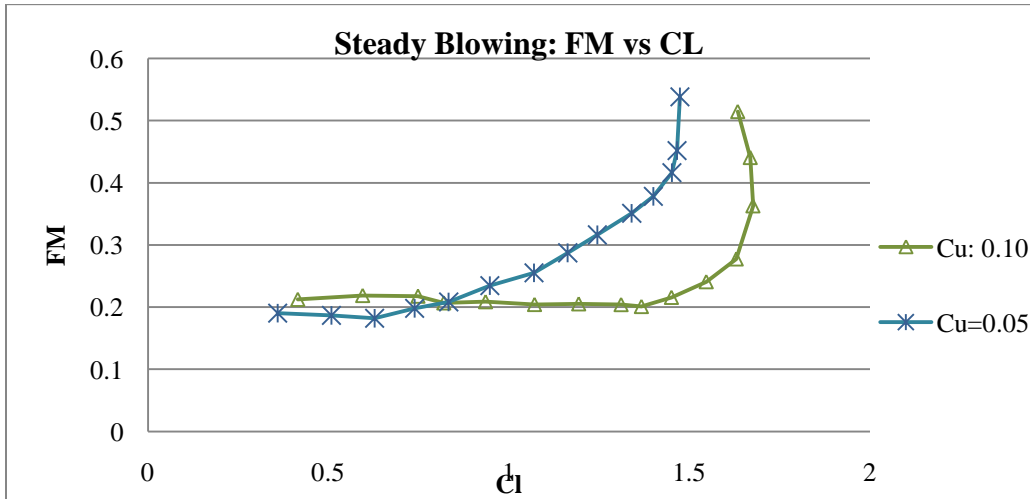


Figure 28 - Figure of Merit plot for two cases of steady blowing AFC

Pulsed blowing and ZMF excitation flow control systems, on the other hand, have demonstrated the ability to reach FM values on the order of 2.5. [12, 6] It is the ability of these system to produce results similar to the ones achieved here using a far lower input energy requirement that as focused such a great deal of attention on pulsed flow control

4.2 Pulsed Results Discussion

Unfortunately the pulsed blowing studies did not provide the same results type of results as the steady cases. As seen in Figures 25 and 26, the pulsed flow control and no discernible impact on the airfoil performance given the experimental uncertainty discussed in Section 2.7. Several factors likely contributed to its limited the effectiveness. The first of these is the nature of the pulses themselves. The longer compressed air supply hoses, bellows, mesh screens and slot geometry all contribute a significant pressure drop and effective air reservoir between the fuel injectors and the leading edge slot. This pressure drop effectively acted as additional inertia within the flow and dampened any large amplitude of fluctuation between the pulse-on jet-velocity and the off-pulse jet velocity.

Furthermore, the peak velocities of the pulsed jet never exceeded 6.5m/s. This is well below the free stream velocity and likely below the majority of the boundary layer velocities given the slot location at only 3.5% cord. As such, it is likely these jets simply did not have the sharp pulse of energy required to briefly accelerate the boundary layer flow and generate the vortices needed for boundary layer flow mixing.

Aside from the nature of the pulses themselves, the geometry of the slot itself may have contributed to the lack of effectiveness in the pulsed cases. While the highly tangential nature of the slot flow proved very effective in the steady blowing cases, the shallow angle of injection

may have limited the interaction between the pulses and the free stream flow. If the effect of the pulses is never able to escape the boundary layer, it is unlikely to be able to induce the vortices needed flow mixing. Without free stream flow mixing, pulsed flow control simply does not inject enough momentum into the boundary layer to overcome the adverse pressure gradient developed at high angles of attack.

5.0 Conclusion

This study was successfully able to evaluate the performance of a leading edge active flow control system in both a pulsed and steady blowing configuration. The experimental setup was shown to be reliable and repeatable as well as able to reproduce the flight characteristics of the unaltered airfoil. Both steady and pulsed AFC were tested at Reynolds numbers of $2.5 \times 10^5 < Re < 5.0 \times 10^5$ with corresponding free stream velocities between 23.3m/s and 16.25m/s. The majority of the analysis done was conducted with respect to the 16.25m/s cases as it offered the widest range of C_μ values available in both steady and pulsed blowing.

Results of the steady blowing cases were very positive. The steady blowing flow control was able to provide a 28.4% increase in the maximum lift generated by the airfoil given a flow control jet with a C_μ of 10%. Interestingly, the highly tangential nature of the jet allowed the airfoil to continue to see improvements in $C_{L\max}$ at very high levels of $C_\mu > 8\%$. Additionally, the steady blowing system was able to increase the airfoil stall angle from 11° to 14° for values of C_μ greater than 3%. While these results certainly demonstrated the benefit of steady state flow control, the drawbacks became apparent in the efficiency analysis. The figures of merit calculations showed that the steady state flow control failed to exceed even a 60% efficiency over the baseline given the amount of input energy required.

The pulsed cases were not able to generate a notable increase in airfoil performance. As discussed, this is most likely due to the small amplitude in jet velocity coupled with the shallow angle of momentum inject into the flow. As a result, the peak jet velocities were not sufficient to excite the boundary layer and create the vortices capable of mixing free stream and boundary layer flows, and therefore was unable to provide the additional momentum needed to postpone separation and stall. Additional work will need to be done to re-configure the compressed air

supply system to deliver larger amplitude pulses while maintaining the desired low mass flow rates.

5.1 Future Work

As discussed, the key element of the study that will require additional work is the pulsed blowing cases. Reconfiguring the compressed air supply apparatus to deliver shaper, larger amplitude pulses would likely deliver results much closer to those seen in the steady blowing cases. As a first step, one should look to minimize the pressure drop between the air injector manifold and the leading edge slot itself. This would be most easily done by removing the fine mesh covering the air supply slots, as well as placing the injectors as close as possible to minimize supply hose lengths. In addition, the use of additional fuel injectors would allow for higher mass flow rates as needed.

The second piece of additional work would be to incorporate a flow visualization system to better understand the nature of the pulses created. A phase locked PIV study examining the duration effect of pulses as well as their ability to travel along the cord would likely give a better understanding of optimal pulse rates and magnitudes.

References

- [1] Budynas, Richard G., J. Keith. Nisbett, and Joseph Edward. Shigley. *Shigley's Mechanical Engineering Design*. Boston: McGraw-Hill, 2008. Print.
- [2] Collis, Scott, Ronald D. Joslin, Avi Seifert, and Vassilis Theofilis. "Issues in Active Flow Control: Theory, Control, Simulation, and Experiment." *Progress in Aerospace Sciences* 40 (2004): 237-89. *Science Direct*. Web.
- [3] Ducloux, Olivier, Yves Deblock, Nicolas Tiercelin, Philippe Pernod, Vladimir Preobrazhensky, and Alain Merlen. "Magnetically Actuated Microvalves for Active Flow Control." *IUTAM Symposium on Flow Control and Mems* 34th ser. (2008): 59-65. *Journal of Physics: Conference Series*. Web. 15 Apr. 2011.
- [4] Dunne, Reeve. "WIND TUNNEL SIMULATION OF FLOW CONTROL WITH PULSED IMPINGING AIR JETS." Thesis. Tufts University, 2011. Print.
- [5] Fox, Robert W., Alan T. McDonald, and Philip J. Pritchard. *Introduction to Fluid Mechanics*. Hoboken, NJ: Wiley, 2009. Print.
- [6] Greenblatt, David, and Isreal J. Wygnanski. "The Control of Flow Separation by Periodic Excitation." *Progress in Aerospace Sciences* 36 (2000): 487-545. *Elsevier*. Web.
- [7] Hsiao, Pei-Bien, Chin-Fung Liu, and Jong-Yaw Shyu. "Control of Wall-Separated Flow by Internal Acoustic Excitation." *American Institute of Aeronautics and Astronautics* 28.8 (1989): 1440-446. Print.
- [8] Jabbal, M., and W. J. Crowther. "Systems and Certification Issues for Civil Transport Aircraft Flow Control Systems." *The Aeronautical Journal* 113.1147 (2009): 575-86. 9 July 2009. Web.
- [9] Magill, John C., and Keith R. McManus. "Exploring the Feasibility of Pulsed Jet Separation Control for Aircraft Configurations." *Journal of Aircraft* 38.1 (2001): 48-56. Web.
- [10] Peitzmeier, Hubert. F104 BLC system schematic. Digital image. *916-Starfighter.de*. Web.
- [11] Scholz, Peter, Jens Ortmanns, Christian J. Kahler, and Rolf Radespiel. "Leading Edge Separation Control by Means of Pulsed Jet Actuators." *American Institute of Aeronautics and Astronautics* 2850 (2006). Print.
- [12] Seifer, A., S. Eliahu, D. Greenblatt, and I. Wygnanski. "Use of Piezoelectric Actuators for Airfoil Separation Control." *American Institute of Aeronautics and Astronautics* 36.8 (1998): 1535-537. Print.

- [13] Seifert, Avi, David Greenblatt, and Israel J. Wignanski. "Active Separation Control: an Overview of Reynolds and Mach Numbers Effects." *Aerospace Science and Technology* 8 (2004): 569-82. Print.
- [14] Stoelinga, Theo. "Information regarding the Lockheed F-104 Starfighter Bleed Air Supply System." Web. <www.xs4all.nl/>.
- [15] Vortex generator installation on a Beech Bonanza wing. Digital image. *Avweb.com*. 13 Nov. 1997. Web.
- [16] Wimpenny, J. C. *The Design and Application of High Lift Devices*. Hatfield, Herts, England: Hawker Siddeley Aviation Limited, 1968. Print.

APPENDIX

Appendix A – Additional Steady Blowing Cases

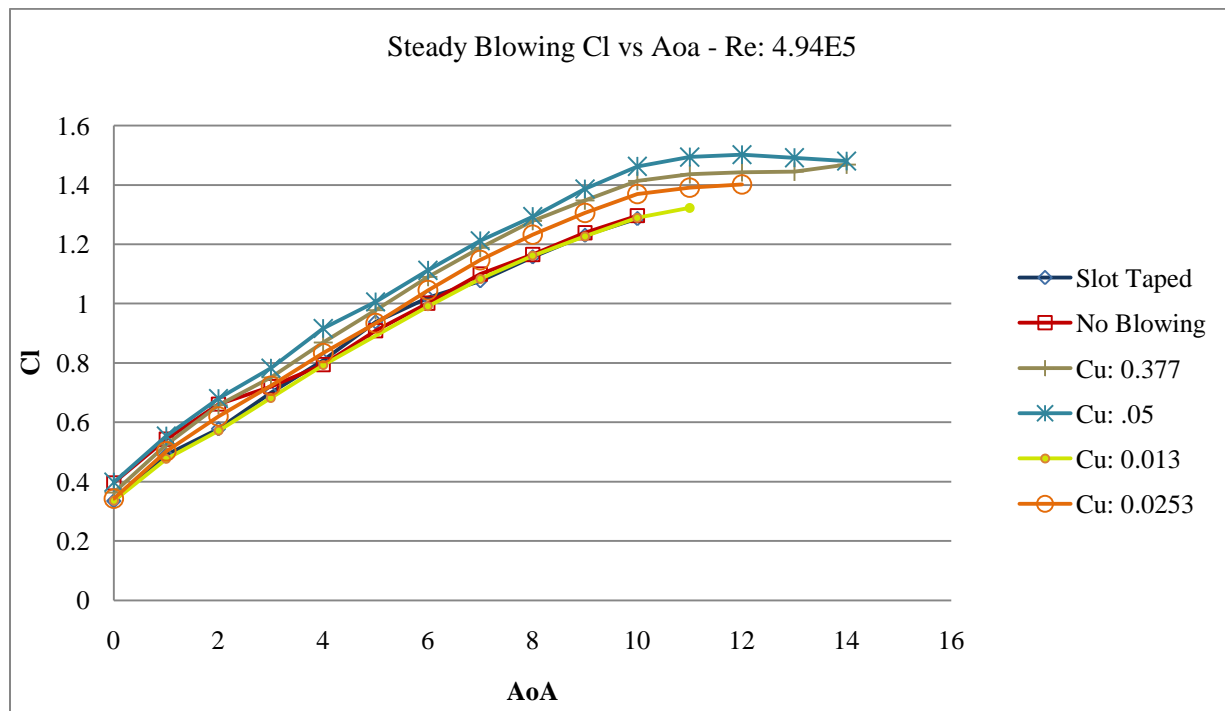


Figure 29 - Steady Blowing $U=23.3\text{m/s}$

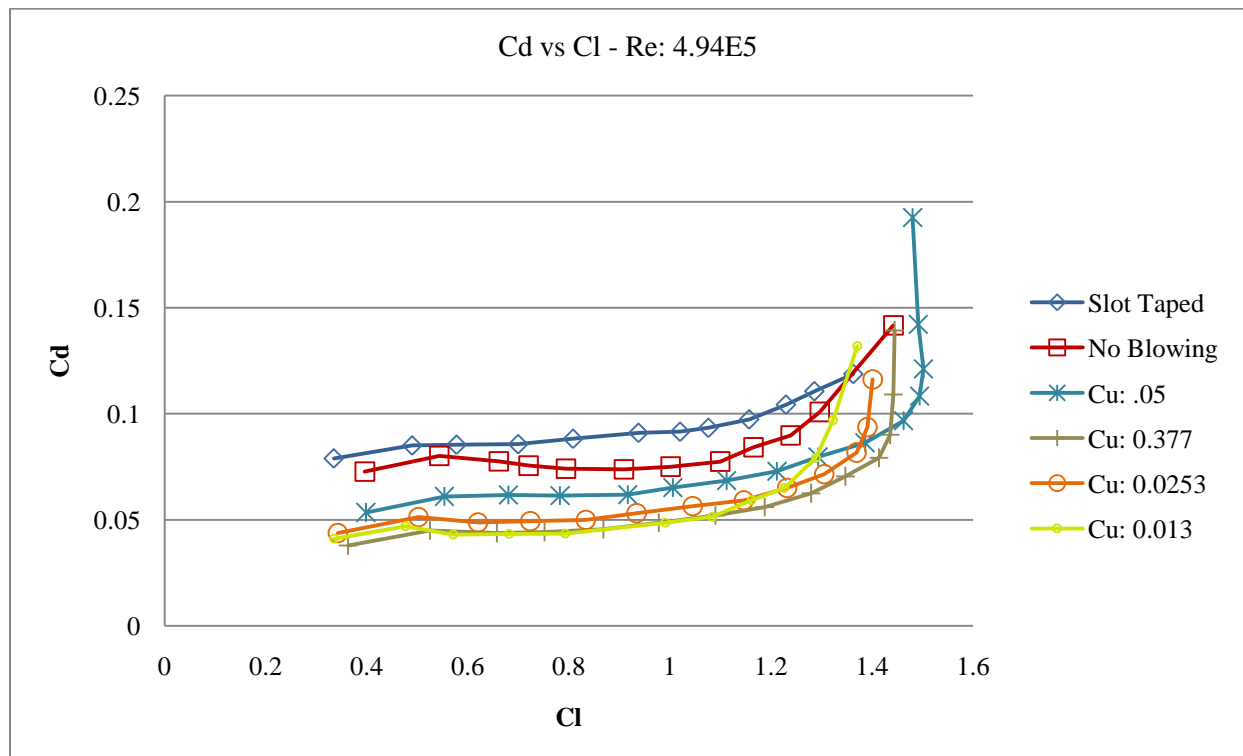


Figure 30 - C_d vs. C_l Steady Blowing cases at $U=23.3\text{ m/s}$

Appendix B – Additional Experimental Setup information

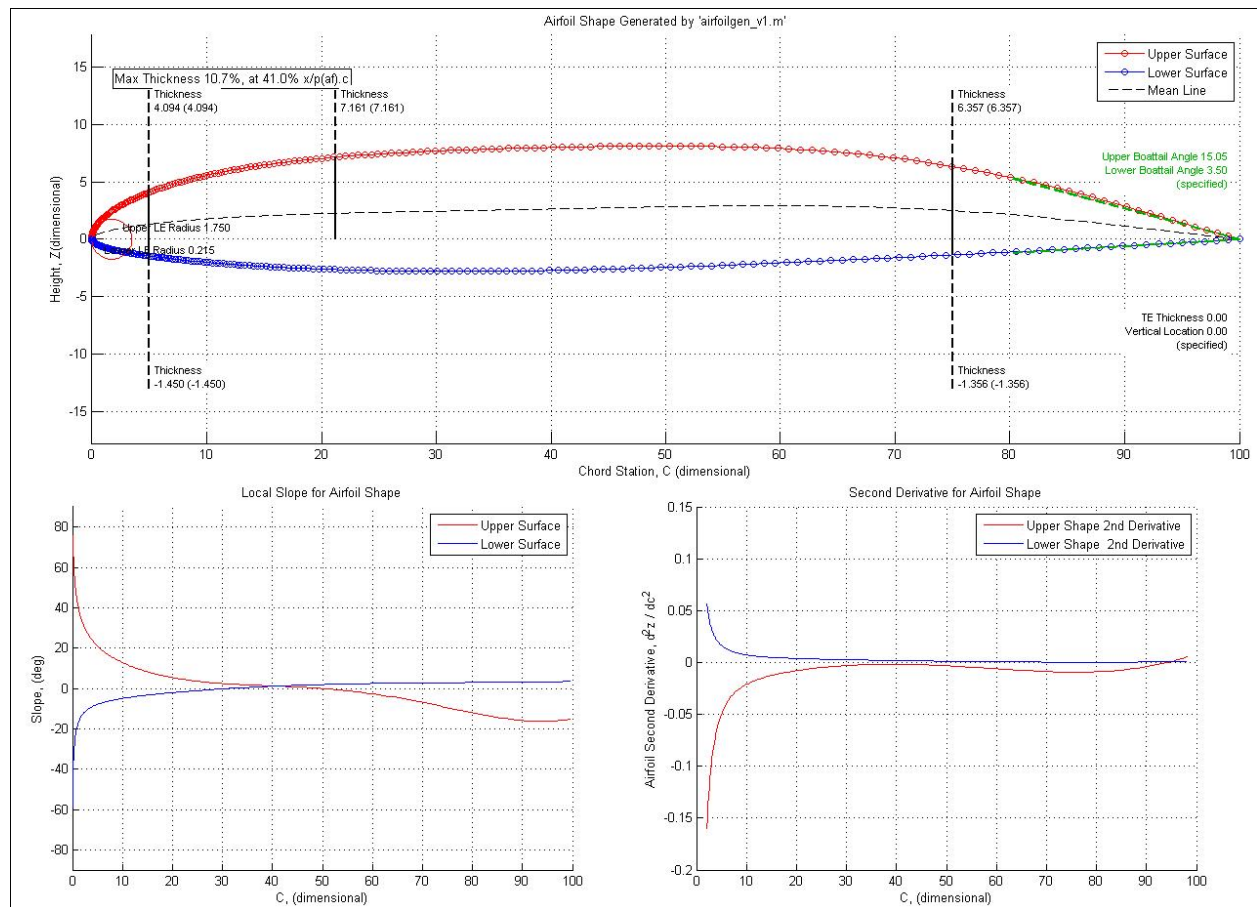
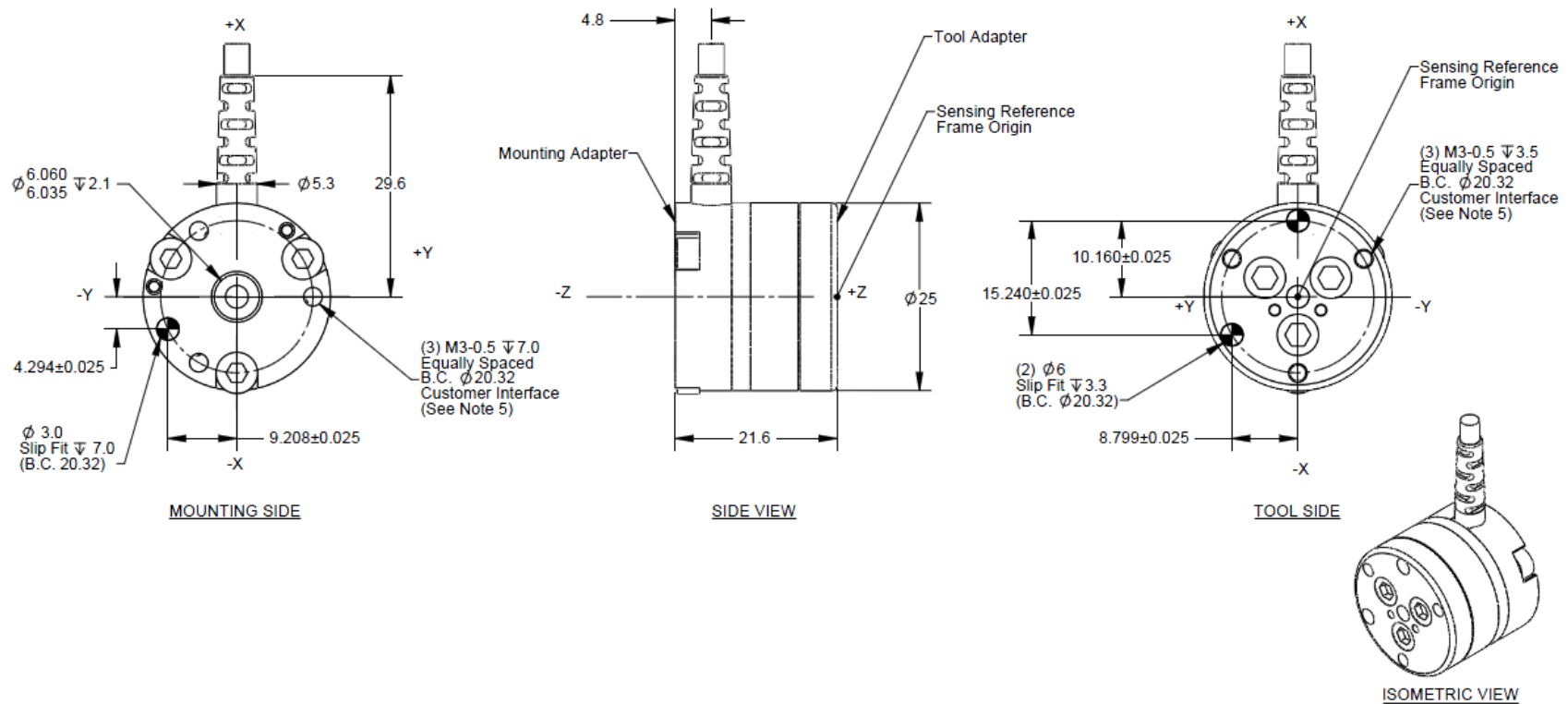


Figure 31 - Additional Airfoil profile Statistics – Northrop Grumman

Rev.	Description	Initiator	Date
01	Initial Drawing	RKC	8/29/2007



Notes:

1. Tool and mounting adapter made of stainless steel. Transducer made of hardened stainless steel.
2. Tool and mounting adapter have M3 tapped holes for interfacing.
3. Connector (not shown) has a 17mm diameter and is 67.5mm long.
4. **WARNING--DO NOT LOOSEN OR REMOVE INTERFACE PLATES DUE TO POTENTIAL DAMAGE.**
5. **DO NOT EXCEED INTERFACE DEPTH--MAY CAUSE DAMAGE.**

NOTES: UNLESS OTHERWISE SPECIFIED
DO NOT SCALE DRAWING. DRAWN IN SOLIDWORKS.
ALL DIMENSIONS ARE IN MILLIMETERS.



1031 Goodworth Drive, Apex, NC 27539, USA
Tel: +1.919.772.0115 Email: info@ati-ia.com
Fax: +1.919.772.8259 www.ati-ia.com
ISO 9001 Registered Company

DRAWN BY: R. Chambers, 8/29/07
CHECKED BY: P. Fusco, 2/22/08
WEIGHT (LB):
ASSEMBLY REF:

Nano25-E Transducer

SCALE: 2:1 SIZE: B DRAWING NUMBER: 9230-05-1312-01

PRODUCT RELEASE # 070118-2 DATE: SHEET 1 OF 1

Figure 32 - ATI Nano25 Drawing

NI 9215

4-Channel, 100 kS/s/ch, 16-bit, ± 10 V Analog Input Module

- 4 simultaneously sampled analog inputs, 100 kS/s
- 16-bit resolution
- Hot-swappable operation
- -40 to 70 °C operating range
- NIST-traceable calibration



Specifications

Specifications Documents

- Specifications
- Data Sheet

Specifications Summary

General	
Product Name	NI 9215
Product Family	Industrial I/O
Form Factor	CompactDAQ , CompactRIO
Part Number	779011-01
Operating System/Target	Real-Time , Windows
Measurement Type	Voltage
Isolation Type	Ch-Earth Ground Isolation
RoHS Compliant	Yes
Analog Input	
Channels	0 , 4
Single-Ended Channels	0

Differential Channels	4
Resolution	16 bits
Sample Rate	100 kS/s
Max Voltage	10 V
Maximum Voltage Range	-10 V , 10 V
Maximum Voltage Range Accuracy	0.003 V
Simultaneous Sampling	Yes
Analog Output	
Channels	0
Digital I/O	
Bidirectional Channels	0
Input-Only Channels	0
Output-Only Channels	0
Number of Channels	0 , 0 , 0
Counter/Timers	
Counters	0
Physical Specifications	
Length	9 cm
Width	2.3 cm
I/O Connector	BNC connectors , Screw terminals
Minimum Operating Temperature	-40 °C
Maximum Operating Temperature	70 °C
Minimum Storage Temperature	-40 °C
Maximum Storage Temperature	85 °C
Timing/Triggering/Synchronization	
Triggers cDAQ Chassis	No

NI 9217

4-Channel, 100 Ω RTD, 24-Bit Analog Input Module

- 4 100 Ω RTD analog inputs
- 24-bit resolution; 50/60 Hz noise rejection
- 3 and 4-wire RTDs; built-in excitation and automatic detection
- Up to 400 S/s sampling rate
- NIST-traceable calibration certificate for guaranteed accuracy



Specifications

Specifications Documents

- Specifications
- Data Sheet

Specifications Summary

General	
Product Name	NI 9217
Product Family	Industrial I/O
Form Factor	CompactDAQ , CompactRIO
Part Number	779592-01
Operating System/Target	Windows , Real-Time
Measurement Type	RTD , Temperature
Isolation Type	Ch-Earth Ground Isolation
RoHS Compliant	Yes
Signal Conditioning	Current excitation
Analog Input	
Channels	0 , 4
Single-Ended Channels	0
Differential Channels	4
Resolution	24 bits

Sample Rate	400 S/s
Simultaneous Sampling	No
Excitation Current	1 mA
Analog Output	
Channels	0
Digital I/O	
Bidirectional Channels	0
Input-Only Channels	0
Output-Only Channels	0
Number of Channels	0 , 0 , 0
Counter/Timers	
Counters	0
Physical Specifications	
Length	9 cm
Width	2.3 cm
I/O Connector	Screw terminals
Minimum Operating Temperature	-40 °C
Maximum Operating Temperature	70 °C
Minimum Storage Temperature	-40 °C
Maximum Storage Temperature	85 °C
Timing/Triggering/Synchronization	
Triggers cDAQ Chassis	No